Monotonicity Preserving Weighted Essentially Non-oscillatory Schemes with Increasingly High Order of Accuracy

Dinshaw Balsara, Chi-Wang Shu

HAL Id: hal-01634261
https://hal.archives-ouvertes.fr/hal-01634261

Submitted on 13 Nov 2017

Monotonicity Preserving Weighted Essentially Non-oscillatory Schemes with Increasingly High Order of Accuracy

Dinshaw S. Balsara[*] and Chi-Wang Shu[†]

[*]*N.C.S.A., University of Illinois at Urbana-Champaign 605 E. Springfield Avenue, Champaign, Illinois 61820; and* [†]*Division of Applied Mathematics, Brown University Providence, Rhode Island 02912*
E-mail: [*]dbalsara@ncsa.uiuc.edu, [†]shu@cfm.brown.edu

In this paper we design a class of numerical schemes that are higher-order extensions of the weighted essentially non-oscillatory (WENO) schemes of G.-S. Jiang and C.-W. Shu (1996) and X.-D. Liu, S. Osher, and T. Chan (1994). Used by themselves, the schemes may not always be monotonicity preserving but coupled with the monotonicity preserving bounds of A. Suresh and H. T. Huynh (1997) they perform very well. The resulting monotonicity preserving weighted essentially non-oscillatory (MPWENO) schemes have high phase accuracy and high order of accuracy. The higher-order members of this family are almost spectrally accurate for smooth problems. Nevertheless, they, have robust shock capturing ability. The schemes are stable under normal CFL numbers. They are also efficient and do not have a computational complexity that is substantially greater than that of the lower-order members of this same family of schemes. The higher accuracy that these schemes offer coupled with their relatively low computational complexity makes them viable competitors to lower-order schemes, such as the older total variation diminishing schemes, for problems containing both discontinuities and rich smooth region structure. We describe the MPWENO schemes here as well as show their ability to reach their designed accuracies for smooth flow. We also examine the role of steepening algorithms such as the artificial compression method in the design of very high order schemes. Several test problems in one and two dimensions are presented. For multidimensional problems where the flow is not aligned with any of the grid directions it is shown that the present schemes have a substantial advantage over lower-order schemes. It is argued that the methods designed here have great utility for direct numerical simulations and large eddy simulations of compressible turbulence. The methodology developed here is applicable to other hyperbolic systems, which is demonstrated by showing

that the MPWENO schemes also work very well on magnetohydrodynamical test problems.

Key Words: conservation law; ENO; weighted ENO; monotonicity preserving; convergence.

I. INTRODUCTION

Ever since the introduction of higher-order Godunov schemes by vanLeer [48] the fluid dynamics community has realized that it is beneficial to strive for schemes of high order of accuracy while retaining the robustness that is common to Godunov-type methods. This especially pertains to spatial accuracy but extends also to temporal accuracy. VanLeer [48] showed that monotonicity preserving versions of the original Godunov [16] scheme that were second-order accurate in space and time could be designed. Colella and Woodward [13] used third-order-accurate interpolants but their scheme was still total variation diminishing (TVD) and, therefore, restricted to being second-order accurate in the L_1 norm even for smooth problems with extrema. Chakravarthy and Osher [11] designed an entire class of TVD schemes with increasing order of accuracy for smooth monotone solutions but these are again only second order for smooth problems with extrema. The monotonicity enforcing limiters in TVD schemes are highly non-linear, making it difficult to remove their deleterious effects on a *post facto* basis. The introduction of essentially non-oscillatory (ENO) schemes by Harten *et al.* [20] showed that (essentially) non-oscillatory schemes of higher than second-order accuracy could be constructed. This initiated a substantial body of research by several authors in the construction of non-oscillatory schemes of higher than second order, one of the more recent being the fifth-order weighted ENO (WENO) scheme of Jiang and Shu [23]. This paper builds on Jiang and Shu [23] and develops an entire class of WENO finite difference schemes with increasing order of accuracy, without a substantial increase in computational complexity.

The early ENO scheme of Harten *et al.* [20] relied on finite volume interpolation. Its multidimensional extension was carried out by Casper [9]. The central idea in these schemes consisted of using the smoothest stencil out of several possible stencils that could cover a given zone in the computational domain and interpolate the solution in that zone with the desired order of accuracy. The stencil was designed to adapt in the vicinity of discontinuities to yield a one-sided interpolation if that became necessary. This gave an essentially non-oscillatory shock transition while maintaining a uniform formal high order of accuracy. High-order (higher than two) finite volume ENO schemes suffered from the fact that the number of stencils that needed to be evaluated grew as the second or third power of the order of interpolation in two and three dimensions, respectively. Also a high-order quadrature is needed to compute the numerical fluxes along cell boundaries. Thus the computational cost of using finite volume ENO schemes in multiple dimensions is quite high. Shu and Osher [38, 39] constructed finite difference ENO schemes based on point values and numerical fluxes. This reduced the number of stencils needed to evaluate so that the number of stencils was only proportional to the order of accuracy of the scheme even in multiple dimensions; it also avoided the need for numerical quadratures for the fluxes. Hence their ENO schemes were more economical than the finite volume versions in multiple dimensions. Time discretization was performed by a class of high-order Runge–Kutta methods that maintained TVD or other stability properties of the spatial operator; see Shu and Osher [38] and Shu [40].

There are many applications of ENO and WENO schemes; see, for example, [41]. Higher-order ENO and WENO schemes are especially suitable for problems containing both shocks and a large number of complex smooth structures, such as compressible hydrodynamic turbulence; see Shu *et al.* [42]. On the other hand, second-order TVD schemes are optimally suited for flow calculations where a small number of isolated shock structures dominate the fluid dynamics.

Liu *et al.* [27] showed that the multiplicity of stencils utilized in an ENO scheme could be used to advantage when all the stencils are smooth to obtain an increase in the order of accuracy of the interpolation. They showed that when the solution was locally smooth enough one could make a convex combination of the stencils in an rth-order ENO scheme to obtain an $(r + 1)$th-order WENO scheme. The weights were designed so that near a discontinuity the scheme is close to ENO, namely stencils crossing discontinuities had nearly zero weights. Jiang and Shu [23] realized that the interpolation methodology had a greater level of freedom than had been realized by Liu *et al.* [27]. An rth-order ENO scheme has r possible stencils that can cover a given cell. It is, therefore, possible to have suitable constant weights for these r stencils so that the resulting linear scheme is $(2r - 1)$th-order accurate when the solution is smooth. Jiang and Shu [23] used these constants for $r = 2$ and $r = 3$, constructed nonlinear weights to achieve the WENO property, and proved that the *nonlinear* WENO schemes for $r = 2$ and $r = 3$ were uniformly third- and fifth-order accurate at all points in the flow including at critical points such as smooth extrema and sonic points. The detailed proof requires one to make analytic expansion of the weighted interpolant with nonlinear weights and has to be proved anew for each value of r that is of interest. Using Mathematica we have been able to show analytically that this uniform $(2r - 1)$th-order accuracy property remains true for $r = 4$ through $r = 7$. The detailed Mathematica proofs have been omitted from this paper to save space. Such accuracy is also verified numerically in Section IV of this paper. The nonlinear weights in the construction of WENO schemes involved a sophisticated measure of the local smoothness, so that when the solution was smooth enough to achieve the maximal attainable order of accuracy it would automatically do so. When the solution was not smooth enough to attain the maximal order of accuracy the smoothness measure would detect such a situation and the scheme would also automatically drop the order of accuracy (but not to lower than rth order). The resulting $r = 3$ WENO scheme was only two to four times as computationally costly as a TVD scheme, depending on the version used. Thus for a complex flow problem the scheme could show its advantage.

Numerical experimentation showed that the $r = 3$ WENO scheme, despite its high accuracy, may still display a considerable dispersion error, especially for long time integrations with very few points per wavelength. Construction of WENO schemes with $r > 3$ has been carried out in this paper. These schemes, when coupled with a third-order Runge–Kutta time discretization, are linearly stable under CFL numbers between 1.43 and 0.99 for $r = 3$ to 7. Higher-order Runge–Kutta methods allow larger CFL numbers for linear stability. For problems where the solution is smooth such schemes achieve their design accuracies, showing them to be potentially useful. Our numerical experiments, however, showed that for problems involving discontinuities, the $r = 5$ WENO used with a temporally third-order accurate Runge–Kutta scheme was non-oscillatory for a CFL number of 0.2 but was already slightly oscillatory for a CFL number of 0.4. The results from these numerical experiments are not shown here to save space. Similar results hold also for high-order ENO schemes, namely, when a high-order spatial discretization is coupled with a lower order Runge–Kutta time stepping, the CFL number should be reduced to be much lower than what is required by

linear stability analysis, not only to keep accuracy but also to keep the non-oscillatory property. Application to other, more challenging hyperbolic systems with more complex wave structure (such as magnetohydrodynamics, MHD) showed that the $r = 3$ WENO scheme with RF or LLF building blocks also had difficulty in handling discontinuities. In another development, Suresh and Huynh [45]—see also the work of Leonard *et al.* [25]—produced a geometrically motivated way of showing that the construction of monotonicity preserving interpolation strategies permitted a greater degree of latitude than had previously been thought possible. Earlier efforts at understanding the monotonicity constraint—see Tadmor [47] or Sweby [46]—were shown to be too restrictive in that they failed to distinguish between a smooth local extremum and a region in the flow with a genuine O(1) discontinuity such as a shock. Suresh and Huynh [45] designed monotonicity preserving bounds on the solution that gets interpolated to the zone boundary that would distinguish between a smooth local extremum and a genuine O(1) discontinuity. The interesting feature of the work of Suresh and Huynh [45] was that their monotonicity bounds could be applied to any higher-order scheme in order to bring it within the monotonicity preserving regime. Application of the monotonicity preserving bounds to the whole class of WENO schemes enabled them to preserve their order of accuracy in regions where it was warranted and yet display stable, oscillation-free behavior for problems where the flow was not smooth. Furthermore, the monotonicity preserving weighted essentially non-oscillatory (MPWENO) schemes were stable for standard Courant numbers. We observe significant improvements in dispersion error as we go from the $r = 3$ WENO scheme to the $r = 6$ MPWENO scheme. The $r = 5$ MPWENO member of this family of schemes is already almost spectrally accurate on a dimension-by-dimension basis; however, our implementation of this scheme on RISC architectures was only 35–50% more expensive than the $r = 3$ WENO scheme. Thus a high level of fidelity is obtained at only a modest increment in computational cost. For certain complex problems the monotonicity preserving mechanism can also cause the MPWENO schemes to have lower formal accuracy than the corresponding WENO schemes. It is shown that the accuracy is, nevertheless, substantially higher than that of older TVD schemes. One of the goals of this paper is to catalogue this family of schemes and their performance. Suresh and Huynh [45] also conjectured that their monotonicity preserving bounds would not degrade the order of accuracy of a numerical scheme. Thus, another goal of this paper is to explore in some detail whether this is uniformly true.

It is well known that contact discontinuities in the linearly degenerate characteristic fields are smeared much more than shocks. The smearing becomes less serious for higher-order schemes. When simple, isolated contact discontinuities are present in the flow two well-established methods of improving the solution exist. The first method is the subcell resolution method of Harten [19]. A similar idea has been extended to multiple dimensions by Fedkiw *et al.* [14] but carries with it considerable computational complexity and therefore is not explored here. The second method is the artificial compression method (ACM) of Harten [17], which was developed in its refined form by Yang [50]. The ACM consisted of improving the steepness of a linearly degenerate characteristic field by adding in an extra piecewise linear profile with magnitude on the level of the local truncation errors of the scheme in smooth regions to the interpolant for that field. The introduction of an extra profile improves the visual structure of an isolated contact discontinuity. We explore the role of the ACM in preserving the order of accuracy for practical problems in this paper. The ACM also has free parameters which control the amount of steepening introduced and we show that higher-order schemes can operate well with smaller values of those parameters,

i.e., with a smaller contribution from the artificial compression method. Based on extensive testing we suggest optimal values of these parameters for MPWENO schemes with $r > 3$.

We would like to stress the importance of higher-order accuracy from the point of view of scientific and engineering applications. This is especially so because the numerical simulation of compressible turbulent flows, perhaps using large eddy simulation (LES) techniques, is becoming increasingly important in science and engineering. For a recent review of LES simulations of compressible flow see Lesieur and Comte [26]. The methods of choice for such simulations seem to be pseudo-spectral methods. However, spectral methods cannot be readily extended to complex geometry, composite grids, and adaptive meshing techniques, and do not degrade gracefully when the full resolution is lost. Higher-order Godunov methods, on the other hand, take well to adaptive mesh refinement; see Burger and Colella [8]. The ability of the methods developed here to take well to complex mesh geometries has also been catalogued in Casper *et al.* [10]. There have been several efforts to analyze the role of numerical accuracy in the simulation of incompressible turbulence flows; see Browning and Kreiss [7] and Ghosal [15] and references therein. A corresponding effort to understand the role of numerical accuracy in the simulation of compressible turbulence flows has not been carried out. However, an examination of the time history of direct numerical simulations (DNS) of decaying compressible hydrodynamical turbulence—see Porter *et al.* [30]—shows that they go through an initial phase where the simulations are dominated by the formation and dissipation of shocks. Once this initial phase is over, the rest of the time history in these simulations is dominated by the formation and evolution of vortical structures, which is quantitatively similar to simulations of decaying incompressible hydrodynamical turbulence. Balsara *et al.* [5] have shown the existence of a similar time history in DNS simulations of compressible MHD turbulence. Thus the results of Browning and Kreiss [7] and Ghosal [15] are also expected to have great relevance to simulations of compressible turbulence. Basing their work on the previous work of Henshaw *et al.* [21], Browning and Kreiss [7] carried out a comparative study of the same DNS simulations of time-evolving turbulence using a second-order finite difference scheme, a fourth-order finite difference scheme, and a pseudo-spectral scheme. They found that for a short period in the time evolution all three simulations agreed with one another. However, for longer time evolution only the results from the fourth-order finite difference scheme and the pseudo-spectral scheme agreed with each other. The errors in the simulation carried out with the second-order scheme built up so rapidly that the results diverged from the correct results after a short period in the time evolution. The result of Browning and Kreiss [7] clearly demonstrates the utility of very high order schemes in simulations of compressible turbulent flows. Ghosal [15] took this study further by focusing on the role of finite difference and pseudo-spectral schemes in LES modeling. The finite difference schemes that Ghosal considered ranged from second-order accurate to eighth-order accurate when viewed on a dimension-by-dimension basis. The power of using higher-order schemes was convincingly demonstrated by Ghosal [15] when he showed that by using an eighth-order accurate finite difference scheme with an LES filter length that was twice as large as the grid scale the numerical errors could be made much smaller than the subgrid force terms on all length scales that were represented in the computation. To achieve a comparable effect from a second-order-accurate finite difference scheme one would have had to set the LES filter length to be eight times as large as the grid scale. A good implementation of the ninth-order accurate $r = 5$ MPWENO scheme reported here is about three times slower than a traditional second-order-accurate TVD scheme. Thus for three-dimensional time-explicit LES

calculations of compressible turbulence, savings by a factor of $4^4/3 = 85.3$ are suggested when the $r = 5$ MPWENO scheme is used instead of a TVD scheme.

In Section II we give some general background information on WENO schemes with the intent of establishing some basic notation. In Section III we give the details of MPWENO interpolation. In Section IV we catalogue the higher-order properties of MPWENO schemes by showing their performance on well-known convergence tests. In Section V we explore the performance of MPWENO schemes when the ACM is used. In Section VI we show the results from several one-dimensional tests. In Section VII we show the results from several multidimensional tests. In Section VIII we draw some conclusions.

II. GENERAL BACKGROUND ON WENO SCHEMES

Consider the hyperbolic system in conservation form given by

$$U_t + \text{div}\, F(U) = 0. \tag{2.1}$$

Here $U = (u_1, \ldots, u_m)$ is the vector of conserved variables, $F(U) = (F_1, \ldots, F_d)$ is a collection of vectors of fluxes, and we work in a d-dimensional space with coordinates $(x_1, \ldots, x_d)$. The problem is specified on a mesh at $t = 0$ and is to be solved for $t > 0$. The temporal discretization is carried out by casting the system in Eq. (2.1) in the form

$$\frac{dU}{dt} = L(U), \tag{2.2}$$

where $L(U)$ is the high-order discrete representation of $-\text{div}\, F(u)$. We then use the TVD Range–Kutta-type methods developed in Shu and Osher [38] to integrate the system in Eq. (2.2) forward in time. Because the temporal update consists of a sum of the discretized derivatives of the fluxes in each direction we restrict our attention to variations in one direction, taken to be the x-direction here. Thus let us discretize the space into zones of size Δx. Let j be an integer, and let x_j denote zone centers and $x_{j+1/2}$ denote zone boundaries. Then one has

$$L(U_j) = -\frac{1}{\Delta x}(\hat{F}_{j+1/2} - \hat{F}_{j-1/2}), \tag{2.3}$$

where $\hat{F}_{j+1/2}$ is a higher-order numerical flux at the $x_{j+1/2}$ zone boundary. Shu and Osher [39] give details on how to use a generating functional approach to produce such a flux and we will not repeat the details here.

The fact that the system is hyperbolic implies that for variations in each coordinate direction there exist an m-dimensional basis of right eigenvectors for the Jacobian in that direction, denoted by $(r_1, \ldots, r_m)$, onto which the solution vector or the flux vector in that direction can be projected. The corresponding left eigenvectors $(l_1, \ldots, l_m)$ are assumed to be orthonormal to the right eigenvectors and help us make this projection. The system admits a set of eigenvalues which we denote by $(\lambda_1, \ldots, \lambda_m)$. All of the LF, LLF, and RF fluxes can be written as projections of different combinations of the fluxes and conserved variables onto the right eigenvectors at the zone boundary $x_{j+1/2}$. The linearized Riemann solver of Roe [33] can be used with U_j and U_{j+1} as the left and right states, respectively, to obtain eigenvalues and right and left eigenvectors at the zone boundary $x_{j+1/2}$. We denote the 5th right and left eigenvectors at the zone boundary $x_{j+1/2}$ by $r_{s;j+1/2}$ and $l_{s;j+1/2}$,

respectively. We also denote the 5th eigenvalue at the zone boundary $x_{j+1/2}$ by $\lambda_{s;j+1/2}$. Then we write the numerical flux at that zone boundary as

$$\hat{F}_{j+1/2} = \sum_{s=1}^{m} (f_{s;j+1/2}^{+} + f_{s;j+1/2}^{-}) \, r_{s;j+1/2}. \tag{2.4}$$

Here $f_{s;j+1/2}^{+}$ and $f_{s;j+1/2}^{-}$ are flux components that are evaluated for each characteristic field s. The flux components assume different values based on the form of the low-order numerical flux that one wishes to employ as a building block for the higher-order ENO or WENO flux. They also depend on the order of accuracy of the interpolation. As shown by Shu and Osher [38, 39], construction of a higher-order ENO scheme entails making a higher-order reconstruction of the flux components obtained from a particular choice of low order numerical flux. In this paper we restrict ourselves to using the LLF or the RF numerical fluxes as the low-order fluxes used as building blocks for the previously mentioned higher-order reconstruction.

In this paragraph we focus on the LLF and RF fluxes that are used as low-order building blocks for pointwise ENO schemes. The first-order LLF flux that one may use as a low-order building block for a higher-order scheme is given by

$$f_{s;j+1/2}^{+} = l_{s;j+1/2} \cdot \frac{1}{2}(F_j + \hat{\lambda}_{s;j+1/2} U_j);$$

$$f_{s;j+1/2}^{-} = l_{s;j+1/2} \cdot \frac{1}{2}(F_{j+1} - \hat{\lambda}_{s;j+1/2} U_{j+1}); \tag{2.5}$$

$$\hat{\lambda}_{s;j+1/2} = \chi \max(|\lambda_{s;j+1/2}|, |\lambda_{s;j}|, |\lambda_{s;j+1}|).$$

Here χ is typically in the range of 1.1 to 1.3 and controls the amount of dissipation introduced into the numerical scheme. Harten [18] has shown the intimate connection between the numerical flux and the dissipation matrix. Because the dissipation introduced by each characteristic field is proportional to the local eigenvalues that belong to that characteristic field the LLF flux is not very dissipative. Besides, as shown by Shu and Osher [39], the higher-order extensions of the ENO schemes built by using the LLF flux as a building block are only marginally more dissipative than the corresponding ENO schemes that use the RF flux as a building block. The first-order RF flux that we have found useful in time-dependent problems as a low-order building block for a higher-order scheme is given by

$$\begin{array}{lll} \text{if } \lambda_{s;j} > 0 & \text{and} & \lambda_{s;j+1} > 0 & \text{then } f_{s;j+1/2}^{+} = l_{s;j+1/2} \cdot F_j; \quad f_{s;j+1/2}^{-} = 0; \\ \text{if } \lambda_{s;j} < 0 & \text{and} & \lambda_{s;j+1} < 0 & \text{then } f_{s;j+1/2}^{+} = 0; \; f_{s;j+1/2}^{-} = l_{s;j+1/2} \cdot F_{j+1}; \\ \text{if } \lambda_{s;j} \leq 0 & \text{and} & \lambda_{s;j+1} \geq 0 & \text{then use Eq. (2.5);} \\ \text{if } \lambda_{s;j} \geq 0 & \text{and} & \lambda_{s;j+1} \leq 0 & \text{then use Eq. (2.5).} \end{array} \tag{2.6a}$$

It is also worthwhile to catalogue the original choice of RF flux in Shu and Osher [39], which was given by

$$\begin{array}{lll} \text{if } \lambda_{s;j} \leq 0 & \text{and} & \lambda_{s;j+1} \geq 0 & \text{then use Eq. (2.5);} \\ \text{else if } \hat{\lambda}_{s;j+1/2} > 0 & & & \text{then } f_{s;j+1/2}^{+} = l_{s;j+1/2} \cdot F_j; \; f_{s;j+1/2}^{-} = 0; \\ \text{else if } \hat{\lambda}_{s;j+1/2} < 0 & & & \text{then } f_{s;j+1/2}^{+} = 0; \; f_{s;j+1/2}^{-} = l_{s;j+1/2} \cdot F_{j+1}. \end{array} \tag{2.6b}$$

Equation (2.6a) introduces an additional dissipation when characteristic fields are flowing into a shock and thus spreads out a shock profile so that it occupies two or three zones. This is a very desirable feature in time-dependent problems. In time-steady problems Eq. (2.6b) has the advantage that it permits the representation of a standing shock with the steepest possible profile. We see that the RF flux simply utilizes the LLF flux when an entropy fix is desired and reduces to a Roe [33] flux when an entropy fix is not needed. Notice that Eqs. (2.5) and (2.6) produce flux components for the flux computation in Eq. (2.4) for each characteristic field of the hyperbolic system. Roe [34] has pointed out that it may be valuable to use different forms of the flux components for different characteristic fields. Based on numerical experiments involving the Euler and MHD systems we have found it valuable to use the LLF flux for linearly degenerate characteristic fields and the RF flux for the genuinely nonlinear characteristic fields. We must remind the reader that Eqs. (2.5) and (2.6) only apply to the construction of first-order-accurate numerical fluxes. In the ensuing paragraphs we will show how they can be used as building blocks for building higher order numerical fluxes.

From Eqs. (2.5) and (2.6) we see that in order to carry out the evaluation of $f^+_{s;\,j+1/2}$ in Eq. (2.4) we necessarily need to utilize the values in the zone that is centered on x_j. There are r candidate stencils that cover this zone each of which can be used to make an rth-order-accurate interpolating function for that zone. We denote these stencils by $S_{j;k}$, where $k = 0, \ldots, r-1$ labels the stencils from the leftmost stencil to the rightmost stencil in that order. One can also graphically illustrate the stencil support by listing the zone centers that are covered by that stencil. Thus for the kth stencil $S_{j;k}$ which interpolates over the zone that is centered on x_j we have

$$S_{j;k} = (x_{j+k-r+1}, x_{j+k-r+2}, \ldots, x_{j+k}). \tag{2.7}$$

Each of the stencils $S_{j;k}$ can provide an rth-order-accurate interpolation at the right boundary of the zone that has x_j as its zone center. Thus if we want the rth-order-accurate interpolation of $f^+_{s;\,j+1/2}$ that can be obtained from the stencil $S_{j;k}$ we need to evaluate the values of the flux components

$$\{f^+_{s;\,j+k-r+1;\,j+1/2},\ f^+_{s;\,j+k-r+2;\,j+1/2},\ \ldots,\ f^+_{s;\,j+k;\,j+1/2}\} \tag{2.8}$$

and use them in the interpolation process. Should we want to use the LLF flux we define the flux components in Eq. (2.8) by

$$f^+_{s;\,j+k;\,j+1/2} = l_{s;\,j+1/2} \cdot \frac{1}{2}(F_{j+k} + \hat{\lambda}_{s;\,j+1/2} U_{j+k});$$
$$\hat{\lambda}_{s;\,j+1/2} = \chi \max(|\lambda_{s;\,j+1/2}|, |\lambda_{s;\,j-r+1}|, \ldots, |\lambda_{s;\,j+r-1}|). \tag{2.9}$$

The second equality in Eq. (2.9) is a little different from $\hat{\lambda}_{s;\,j+1/2} = \chi \max(|\lambda_{s;\,j}|, |\lambda_{s;\,j+1}|)$, which was the choice for that formula that was catalogued in Shu and Osher [39]. Our choice in Eq. (2.9) has a little better dependence on the particular stencil being used and provides the numerical scheme with much more robustness at reflecting boundaries. Should we want

to use the RF flux we define the flux components in Eq. (2.8) in analogy with Eq. (2.6a) by

$$
\begin{aligned}
&\text{if } \lambda_{s;j} > 0 \quad \text{and} \quad \lambda_{s;j+1} > 0 \qquad \text{then } f^+_{s;j+k;j+1/2} = l_{s;j+1/2} \cdot F_{j+k}; \\
&\text{if } \lambda_{s;j} < 0 \quad \text{and} \quad \lambda_{s;j+1} < 0 \qquad \text{then } f^+_{s;j+k;j+1/2} = 0; \\
&\text{if } \lambda_{s;j} \leq 0 \quad \text{and} \quad \lambda_{s;j+1} \geq 0 \qquad \text{then use Eq. (2.9);} \\
&\text{if } \lambda_{s;j} \geq 0 \quad \text{and} \quad \lambda_{s;j+1} \leq 0 \qquad \text{then use Eq. (2.9);}
\end{aligned} \tag{2.10a}
$$

The variant of Eq. (2.10a) which is analogous to Eq. (2.6b) is given by

$$
\begin{aligned}
&\text{if } \lambda_{s;j} \leq 0 \quad \text{and} \quad \lambda_{s;j+1} \geq 0 \qquad \text{then use Eq. (2.9);} \\
&\text{else if } \hat{\lambda}_{s;j+1/2} > 0 \qquad\qquad\qquad \text{then } f^+_{s;j+k;j+1/2} = l_{s;j+1/2} \cdot F_{j+k}; \\
&\text{else if } \hat{\lambda}_{s;j+1/2} < 0 \qquad\qquad\qquad \text{then } f^+_{s;j+k;j+1/2} = 0.
\end{aligned} \tag{2.10b}
$$

When each of the stencils $S_{j;k}$ has a smooth solution we can make a convex combination of the interpolated values that we obtain from each of the r stencils in order to obtain a $(2r-1)^{\text{th}}$-order-accurate evaluation of the interpolated value of the flux components at the point $x_{j+1/2}$.

We now give the details of the interpolation process. Specifically, we are interested in making a $(2r-1)^{\text{th}}$-order-accurate evaluation of the interpolated value at the point $x_{j+1/2}$, which constitutes the right boundary of the interpolated zone that is centered on x_j. The rth-order-accurate value that can be obtained by the reconstruction using the kth stencil $S_{j;k}$ is denoted by $q^{+r}_{s;j;k}$ ($f^+_{s;j+k-r+1;j+1/2}, f^+_{s;j+k-r+2;j+1/2}, \ldots, f^+_{s;j+k;j+1/2}$). It can be written as a linear combination of the values in Eq. (2.8). We write it explicitly as

$$
q^{+r}_{s;j;k}(f^+_{s;j+k-r+1;j+1/2}, f^+_{s;j+k-r+2;j+1/2}, \ldots, f^+_{s;j+k;j+1/2}) = \sum_{i=1}^{r} a^r_{k;i} f^+_{s;j+k-r+i;j+1/2}. \tag{2.11}
$$

The constant coefficients $a^r_{k;i}$ for $r=4$ through $r=7$ will be tabulated in the next section. Since $k=0, \ldots, r-1$ in Eq. (2.11) there are r possible stencils and, therefore, r possible interpolated values that we may obtain from Eq. (2.11). When the solution is smooth the $(2r-1)^{\text{th}}$-order-accurate evaluation of the interpolated value at the point $x_{j+1/2}$ is obtained by making a convex combination of the r possible values that we may obtain from Eq. (2.11). This can be written as

$$
f^+_{s;j+1/2} = \sum_{k=0}^{r-1} C^r_k \, q^{+r}_{s;j;k}(f^+_{s;j+k-r+1;j+1/2}, f^+_{s;j+k-r+2;j+1/2}, \ldots, f^+_{s;j+k;j+1/2}) \tag{2.12}
$$

Thus for each value of r there exist r positive coefficients C^r_k which can be used to improve the local accuracy at a selected point. We refer to these coefficients as the optimal weights. Equation (2.12) is still not suitable for use in Eq. (2.4) for the following reason. When the solution is adequately smooth we want the interpolation to achieve its maximal $(2r-1)^{\text{th}}$-order accuracy. When this is not the case we wish to automatically put the burden of interpolation on the one or more smoothest stencils out of the r possible stencils. Thus we need an estimator for the smoothness of a stencil. We denote this smoothness estimator

by IS_k^r. Details about the design of these smoothness indicators have been given in Jiang and Shu [23]. They can be constructed for all values of r and we have carried out such a construction for $r = 4$ through $r = 7$. Using these smoothness estimators we can write an equation that is analogous to Eq. (2.12), which is what we use in Eq. (2.4). Thus we have

$$f_{s;j+1/2}^+ = \sum_{k=0}^{r-1} \omega_k^r \, q_{s;j;k}^{+r} (f_{s;j+k-r+1;j+1/2}^+, \, f_{s;j+k-r+2;j+1/2}^+, \dots, \, f_{s;j+k;j+1/2}^+), \quad (2.13)$$

where the coefficients ω_k^r depend on the smoothness measures IS_k^r. The coefficients ω_k^r are designed so that they approximate C_k^r to within $(\Delta x)^{r-1}$ when all the stencils have a smooth solution. This ensures that we can achieve the maximal $(2r-1)^{\text{th}}$ order of accuracy when it is warranted. The actual construction of the weights goes as follows

$$\omega_k^r = \frac{\alpha_k^r}{\alpha_0^r + \cdots + \alpha_{r-1}^r}, \quad (2.14)$$

where

$$\alpha_k^r = \frac{C_k^r}{(\varepsilon + IS_k^r)^p}. \quad (2.15)$$

Here we set $\varepsilon = 10^{-10}$ to avoid division by zero. We also find that $p = 2$ works well. This completes the discussion of the WENO interpolation process.

III. MPWENO INTERPOLATION

The discussion in the previous section shows that we need a tabulation of the coefficients $a_{k;i}^r$ in Eq. (2.11), the smoothness estimators IS_k^r, and the optimal weights C_k^r in order to design MPWENO schemes of increasingly high order of accuracy. We tabulate these coefficients here for $r = 4$ through $r = 6$. The corresponding information for $r = 2$ and $r = 3$ was given in Jiang and Shu [23]. The indices in Eqs. (2.11) and (2.13) are rather complicated and thus are difficult to carry around in all the expressions in this section. Thus, in this section, we give the details of interpolating a scalar quantity u to the right boundary of a zone centered on x_j and we denote this interpolated value of u as $u_{j+1/2}^L$.

In some circumstances and for some hyperbolic systems, like incompressible flow, the flow may be very smooth. In these cases the computation of the smoothness estimators can be bypassed entirely. It may then become computationally efficient to evaluate $u_{j+1/2}^L$ using just the optimal weights in Eq. (2.12). When this is done, simple closed form expressions for $u_{j+1/2}^L$ in terms of the values on a $(2r-1)$ point stencil can be easily obtained. In what follows we also give such expressions.

When the smoothness indicators are evaluated, carrying out the WENO interpolation for a given r requires $r^3 + 4r^2 + 2r$ float point operations. Thus the $r = 5$ WENO scheme interpolation requires about thrice as many float point operations as the $r = 3$ WENO scheme. In practice, there are other steps such as eigenvector construction and characteristic projection which depend on the hyperbolic system being solved and determine the real cost of the scheme. Furthermore, on RISC processors, the interpolation step for larger values of r provides many more opportunities for cache reuse than the interpolation step for lower

TABLE I

$a_{k;i}^4$ values	$i=1$	$i=2$	$i=3$	$i=4$
$k=0$	$-1/4$	$13/12$	$-23/12$	$25/12$
$k=1$	$1/12$	$-5/12$	$13/12$	$1/4$
$k=2$	$-1/12$	$7/12$	$7/12$	$-1/12$
$k=3$	$1/4$	$13/12$	$-5/12$	$1/12$

values of r. For such reasons the $r=5$ WENO/MPWENO scheme takes only 35–50% more time than the $r=3$ WENO scheme in our implementation.

III.a. *Coefficients and Smoothness Estimators for $r=4$*

Table I gives the coefficients for the $r=4$ case. The smoothness estimators are given by

$$IS_0^4 = u_{j-3}(547u_{j-3} - 3882u_{j-2} + 4642u_{j-1} - 1854u_j) + u_{j-2}(7043u_{j-2} - 17246u_{j-1}$$
$$+ 7042u_j) + u_{j-1}(11003u_{j-1} - 9402u_j) + 2107u_j^2$$

$$IS_1^4 = u_{j-2}(267u_{j-2} - 1642u_{j-1} + 1602u_j - 494u_{j+1}) + u_{j-1}(2843u_{j-1} - 5966u_j$$
$$+ 1922u_{j+1}) + u_j(3443u_j - 2522u_{j+1}) + 547u_{j+1}^2$$

$$IS_2^4 = u_{j-1}(547u_{j-1} - 2522u_j + 1922u_{j+1} - 494u_{j+2}) + u_j(3443u_j - 5966u_{j+1}$$
$$+ 1602u_{j+2}) + u_{j+1}(2843u_{j+1} - 1642u_{j+2}) + 267u_{j+2}^2$$

$$IS_3^4 = u_j(2107u_j - 9402u_{j+1} + 7042u_{j+2} - 1854u_{j+3}) + u_{j+1}(11003u_{j+1} - 17246u_{j+2}$$
$$+ 4642u_{j+3}) + u_{j+2}(7043u_{j+2} - 3882u_{j+3}) + 547u_{j+3}^2.$$

The optimal weights are given by

$$C_0^4 = 1/35; \qquad C_1^4 = 12/35; \qquad C_2^4 = 18/35; \qquad C_3^4 = 4/35$$

Evaluating $u_{j+1/2}^L$ using just the optimal weights we get

$$u_{j+1/2}^L = -(1/140)u_{j-3} + (5/84)u_{j-2} - (101/420)u_{j-1} + (319/420)u_j$$
$$+ (107/210)u_{j+1} - (19/210)u_{j+2} + (1/105)u_{j+3}.$$

III.b. *Coefficients and Smoothness Estimators for $r=5$*

Table II gives the coefficients for the $r=5$ case. The smoothness estimators are given by

$$IS_0^5 = u_{j-4}(22658u_{j-4} - 208501u_{j-3} + 364863u_{j-2} - 288007u_{j-1} + 86329u_j)$$
$$+ u_{j-3}(482963u_{j-3} - 1704396u_{j-2} + 1358458u_{j-1} - 411487u_j)$$
$$+ u_{j-2}(1521393u_{j-2} - 2462076u_{j-1} + 758823u_j)$$
$$+ u_{j-1}(1020563u_{j-1} - 649501u_j) + 107918u_j^2$$

TABLE II

$a_{k;i}^5$ values	$i=1$	$i=2$	$i=3$	$i=4$	$i=5$
$k=0$	1/5	−21/20	137/60	−163/60	137/60
$k=1$	−1/20	17/60	−43/60	77/60	1/5
$k=2$	1/30	−13/60	47/60	9/20	−1/20
$k=3$	−1/20	9/20	47/60	−13/60	1/30
$k=4$	1/5	77/60	−43/60	17/60	−1/20

$$
\begin{aligned}
IS_1^5 =\ & u_{j-3}(6908u_{j-3} - 60871u_{j-2} + 99213u_{j-1} - 70237u_j + 18079u_{j+1}) \\
& + u_{j-2}(138563u_{j-2} - 464976u_{j-1} + 337018u_j - 88297u_{j+1}) \\
& + u_{j-1}(406293u_{j-1} - 611976u_j + 165153u_{j+1}) \\
& + u_j(242723u_j - 140251u_{j+1}) + 22658u_{j+1}^2
\end{aligned}
$$

$$
\begin{aligned}
IS_2^5 =\ & u_{j-2}(6908u_{j-2} - 51001u_{j-1} + 67923u_j - 38947u_{j+1} + 8209u_{j+2}) \\
& + u_{j-1}(104963u_{j-1} - 299076u_j + 179098u_{j+1} - 38947u_{j+2}) \\
& + u_j(231153u_j - 299076u_{j+1} + 67923u_{j+2}) \\
& + u_{j+1}(104963u_{j+1} - 51001u_{j+2}) + 6908u_{j+2}^2
\end{aligned}
$$

$$
\begin{aligned}
IS_3^5 =\ & u_{j-1}(22658u_{j-1} - 140251u_j + 165153u_{j+1} - 88297u_{j+2} + 18079u_{j+3}) \\
& + u_j(242723u_j - 611976u_{j+1} + 337018u_{j+2} - 70237u_{j+3}) \\
& + u_{j+1}(406293u_{j+1} - 464976u_{j+2} + 99213u_{j+3}) \\
& + u_{j+2}(138563u_{j+2} - 60871u_{j+3}) + 6908u_{j+3}^2
\end{aligned}
$$

$$
\begin{aligned}
IS_4^5 =\ & u_j(107918u_j - 649501u_{j+1} + 758823u_{j+2} - 411487u_{j+3} + 86329u_{j+4}) \\
& + u_{j+1}(1020563u_{j+1} - 2462076u_{j+2} + 1358458u_{j+3} - 288007u_{j+4}) \\
& + u_{j+2}(1521393u_{j+2} - 1704396u_{j+3} + 364863u_{j+4}) \\
& + u_{j+3}(482963u_{j+3} - 208501u_{j+4}) + 22658u_{j+4}^2.
\end{aligned}
$$

The optimal weights are given by

$$
C_0^5 = 1/126; \qquad C_1^5 = 10/63; \qquad C_2^5 = 10/21; \qquad C_3^5 = 20/63; \qquad C_4^5 = 5/126.
$$

Evaluating $u_{j+1/2}^L$ using just the optimal weights we get

$$
\begin{aligned}
u_{j+1/2}^L =\ & (1/630)u_{j-4} - (41/2520)u_{j-3} + (199/2520)u_{j-2} - (641/2520)u_{j-1} \\
& + (1879/2520)u_j + (275/504)u_{j+1} - (61/504)u_{j+2} \\
& + (11/504)u_{j+3} - (1/504)u_{j+4}.
\end{aligned}
$$

TABLE III

$a_{k;i}^6$ values	$i=1$	$i=2$	$i=3$	$i=4$	$i=5$	$i=6$
$k=0$	$-1/6$	$31/30$	$-163/60$	$79/20$	$-71/20$	$49/20$
$k=1$	$1/30$	$-13/60$	$37/60$	$-21/20$	$29/20$	$1/6$
$k=2$	$-1/60$	$7/60$	$-23/60$	$19/20$	$11/30$	$-1/30$
$k=3$	$1/60$	$-2/15$	$37/60$	$37/60$	$-2/15$	$1/60$
$k=4$	$-1/30$	$11/30$	$19/20$	$-23/60$	$7/60$	$-1/60$
$k=5$	$1/6$	$29/20$	$-21/20$	$37/60$	$-13/60$	$1/30$

III.c. *Coefficients and Smoothness Estimators for $r = 6$*

Table III gives the coefficients for the $r = 6$ case. The smoothness estimators are given by

$$
\begin{aligned}
IS_0^6 = & \; u_{j-5}(1152561u_{j-5} - 12950184u_{j-4} + 29442256u_{j-3} - 33918804u_{j-2} \\
& + 19834350u_{j-1} - 4712740u_j) + u_{j-4}(36480687u_{j-4} - 166461044u_{j-3} \\
& + 192596472u_{j-2} - 113206788u_{j-1} + 27060170u_j) \\
& + u_{j-3}(190757572u_{j-3} - 444003904u_{j-2} + 262901672u_{j-1} - 63394124u_j) \\
& + u_{j-2}(260445372u_{j-2} - 311771244u_{j-1} + 76206736u_j) \\
& + u_{j-1}(94851237u_{j-1}) - 47460464u_j) + 6150211u_j^2
\end{aligned}
$$

$$
\begin{aligned}
IS_1^6 = & \; u_{j-4}(271779u_{j-4} - 3015728u_{j-3} + 6694608u_{j-2} - 7408908u_{j-1} + 4067018u_j \\
& - 880548u_{j+1}) + u_{j-3}(8449957u_{j-3} - 37913324u_{j-2} + 42405032u_{j-1} \\
& - 23510468u_j + 5134574u_{j+1}) + u_{j-2}(43093692u_{j-2} - 97838784u_{j-1} \\
& + 55053752u_j - 12183636u_{j+1}) + u_{j-1}(56662212u_{j-1} - 65224244u_j \\
& + 14742480u_{j+1}) + u_j(19365967u_j - 9117992u_{j+1}) + 1152561u_{j+1}^2
\end{aligned}
$$

$$
\begin{aligned}
IS_2^6 = & \; u_{j-3}(139633u_{j-3} - 1429976u_{j-2} + 2863984u_{j-1} - 2792660u_j + 1325006u_{j+1} \\
& - 245620u_{j+2}) + u_{j-2}(3824847u_{j-2} - 15880404u_{j-1} + 15929912u_j \\
& - 7727988u_{j+1} + 1458762u_{j+2}) + u_{j-1}(17195652u_{j-1} - 35817664u_j \\
& + 17905032u_{j+1} - 3462252u_{j+2}) + u_j(19510972u_j - 20427884u_{j+1} \\
& + 4086352u_{j+2}) + u_{j+1}(5653317u_{j+1} - 2380800u_{j+2}) + 271779u_{j+2}^2
\end{aligned}
$$

$$
\begin{aligned}
IS_3^6 = & \; u_{j-2}(271779u_{j-2} - 2380800u_{j-1} + 4086352u_j - 3462252u_{j+1} + 1458762u_{j+2} \\
& - 245620u_{j+3}) + u_{j-1}(5653317u_{j-1} - 20427884u_j + 17905032u_{j+1} \\
& - 7727988u_{j+2} + 1325006u_{j+3}) + u_j(19510972u_j - 35817664u_{j+1} \\
& + 15929912u_{j+2} - 2792660u_{j+3}) + u_{j+1}(17195652u_{j+1} - 15880404u_{j+2} \\
& + 2863984u_{j+3}) + u_{j+2}(3824847u_{j+2} - 1429976u_{j+3}) + 139633u_{j+3}^2
\end{aligned}
$$

$$IS_4^6 = u_{j-1}(1152561u_{j-1} - 9117992u_j + 14742480u_{j+1} - 12183636u_{j+2}$$
$$+ 5134574u_{j+3} - 880548u_{j+4}) + u_j(19365967u_j - 65224244u_{j+1}$$
$$+ 55053752u_{j+2} - 23510468u_{j+3} + 4067018u_{j+4})$$
$$+ u_{j+1}(56662212u_{j+1} - 97838784u_{j+2} + 42405032u_{j+3} - 7408908u_{j+4})$$
$$+ u_{j+2}(43093692u_{j+2} - 37913324u_{j+3} + 6694608u_{j+4})$$
$$+ u_{j+3}(8449957u_{j+3} - 3015728u_{j+4}) + 271779u_{j+4}^2$$

$$IS_5^6 = u_j(6150211u_j - 47460464u_{j+1} + 76206736u_{j+2} - 63394124u_{j+3} + 27060170u_{j+4}$$
$$- 4712740u_{j+5}) + u_{j+1}(94851237u_{j+1} - 311771244u_{j+2} + 262901672u_{j+3}$$
$$- 113206788u_{j+4} + 19834350u_{j+5}) + u_{j+2}(260445372u_{j+2} - 444003904u_{j+3}$$
$$+ 192596472u_{j+4} - 33918804u_{j+5}) + u_{j+3}(190757572u_{j+3} - 166461044u_{j+4}$$
$$+ 29442256u_{j+5}) + u_{j+4}(36480687u_{j+4} - 12950184u_{j+5}) + 1152561u_{j+5}^2.$$

The optimal weights are given by

$$C_0^6 = 1/462; \quad C_1^6 = 5/77; \quad C_2^6 = 25/77; \quad C_3^6 = 100/231;$$
$$C_4^6 = 25/154; \quad C_5^6 = 1/77.$$

Evaluating $u_{j+1/2}^L$ using just the optimal weights we get

$$u_{j+1/2}^L = -(1/2772)u_{j-5} + (61/13860)u_{j-4} - (703/27720)u_{j-3} + (371/3960)u_{j-2}$$
$$- (7303/27720)u_{j-1} + (20417/27720)u_j + (15797/27720)u_{j+1}$$
$$- (4003/27720)u_{j+2} + (947/27720)u_{j+3} - (17/3080)u_{j+4} + (1/2310)u_{j+5}.$$

III.d. *Monotonicity Preserving Bounds*

Suresh and Huynh [45] found a general way of bounding the value $u_{j+1/2}^L$ so that the bounded value is monotonicity preserving. The key idea in that work was that one must distinguish between smooth local extrema and a genuine O(1) discontinuity. Like Chakravarthy and Osher [11] and Harten *et al.* [20] before them, Suresh and Huynh [45] realized that it was essentially the clipping of local extrema that causes a loss of order of accuracy and must, therefore, be avoided in the design of higher-order schemes. Local extrema are distinguished by analyzing the local curvature in the weights for a particular characteristic field. Should a local extremum be detected enough space was created to allow for the local extremum to be accommodated in the evaluation of $u_{j+1/2}^L$. We catalogue the formulae for bringing $u_{j+1/2}^L$ within the monotonicity preserving bounds here for three reasons: (1) We have found it valuable to use values somewhat different from those in Suresh and Huynh [45]. (2) There is a slightly greater latitude of freedom in the design of these monotonicity preserving bounds which we have found useful in the treatment of certain types of hyperbolic systems and we wish to catalogue it here. (3) In the following section we wish to evaluate the effect of different types of monotonicity bounds that can be designed on the order property of MPWENO schemes.

Following Suresh and Huynh [45] we focus on local measures of curvature here. In order to utilize them in a numerical code we need to define the minmod and median functions as

$$\text{minmod}(x, y) = \frac{1}{2}(\text{sgn}(x) + \text{sgn}(y)) \min(|x|, |y|) \tag{3.1}$$

$$\text{median}(x, y, z) = x + \text{minmod}(y - x, z - x). \tag{3.2}$$

It then becomes useful to define the curvature measures at the zone centers as

$$d_j = u_{j+1} - 2u_j + u_{j-1}. \tag{3.3}$$

The expressions in Eq. (3.3) can be used to define the curvature at the zone boundary. This is where a variety of definitions become possible. The definition of the curvature at the zone boundary which is least restrictive in that it provides maximal space for local extrema to develop is given by

$$d_{j+1/2}^{\text{MM}} = \text{minmod}(d_j, d_{j+1}) \tag{3.4}$$

The superscript MM in Eq. (3.4) indicates the use of the minmod function. Suresh and Huynh [45] recommend using a measure of the curvature at the zone boundary that is somewhat more restrictive in that it reduces the space for local extrema to develop when the ratio d_{j+1}/d_j is larger than 4 or smaller than 1/4 (hence the use of the superscript M4 in the ensuing equation). It is given by

$$d_{j+1/2}^{\text{M4}} = \text{minmod}(4d_j - d_{j+1}, \, 4d_{j+1} - d_j, \, d_j, \, d_{j+1}). \tag{3.5}$$

The choice of the range [1/4, 4] in Eq. (3.5) is one of the heuristic features in the design of monotonicity preserving schemes. In the next section we will show that the resulting schemes are not sensitively dependent on this choice. It is interesting to notice that Eqs. (3.4) and (3.5) would admit any situation where two zones had the same curvature as being an acceptable extremum. For certain hyperbolic systems, MHD being a case in point, the presence of small scale extrema where the wiggles in the solution are spread over just four zones can damage the quality of the solution. In this case it becomes useful to admit only those extrema where the profile of the extremal solution has a slightly larger domain of support. Thus without damaging the monotonicity preserving character of the interpolation strategy we can write this measure of the curvature with extended (denoted by superscript M4X) domain of support as

$$d_{j+1/2}^{\text{M4X}} = \text{minmod}(4d_j - d_{j+1}, \, 4d_{j+1} - d_j, \, d_j, \, d_{j+1}, \, d_{j-1}, \, d_{j+2}) \tag{3.6}$$

In the following section we will demonstrate that Eq. (3.6) performs almost as well as Eq. (3.5).

Following Suresh and Huynh [45] we wish to define minimum and maximum bounds, denoted by $u_{j+1/2}^{\text{L,min}}$ and $u_{j+1/2}^{\text{L,max}}$, within which the solution $u_{j+1/2}^{\text{L}}$ has to lie. The left-sided upper limit (denoted by superscript UL) to the solution at $x_{j+1/2}$ is given by

$$u_{j+1/2}^{\text{UL}} = u_j + \alpha(u_j - u_{j-1}). \tag{3.7}$$

The value of α determines the CFL number that can be used with the scheme. In theory the CFL number is required to be less than $1/(1+\alpha)$. In practice we have found that $\alpha = 2$ allows us to safely use a CFL number of 0.6 in a large number of test problems that we have tried. For superlative treatment of advected pulses a CFL number closer to 0.33 is, however, recommended. The median (denoted by superscript MD) value of the solution at $x_{j+1/2}$ is given by

$$u^{\text{MD}}_{j+1/2} = \frac{1}{2}(u_j + u_{j+1}) - \frac{1}{2}d^{\text{MD}}_{j+1/2}. \tag{3.8}$$

The left-sided value with allowance made for a large curvature (denoted by superscript LC) in the solution at $x_{j+1/2}$ is given by

$$u^{\text{LC}}_{j+1/2} = u_j + \frac{1}{2}(u_j - u_{j-1}) + \frac{\beta}{3}d^{\text{LC}}_{j-1/2}. \tag{3.9}$$

The value of β determines the amount of freedom available from utilizing a large value for the local curvature. We have found that $\beta = 4$ works well for the schemes presented here. We have also found that $\beta = 2$ does not degrade the order property so that the MPWENO schemes presented here are not sensitively dependent on the value of β. This is very satisfying because the value of β is one of the heuristic factors in the design of monotonicity preserving schemes. For all the tests reported here we have used $\beta = 4$. We find that setting $d^{\text{MD}}_{j+1/2} = d^{\text{LC}}_{j+1/2} = d^{\text{MM}}_{j+1/2}$ provides the maximal space for local extrema to develop. Setting $d^{\text{MD}}_{j+1/2} = d^{\text{LC}}_{j+1/2} = d^{\text{M4}}_{j+1/2}$, which is also the choice that was made in Suresh and Huynh [45], somewhat limits the space available for local extrema to develop. Setting $d^{\text{MD}}_{j+1/2} = d^{\text{LC}}_{j+1/2} = d^{\text{M4X}}_{j+1/2}$ filters out extremal features that have a very small domain of support but leaves extremal features with larger support intact. Expressions for $u^{\text{L,min}}_{j+1/2}$ and $u^{\text{L,max}}_{j+1/2}$ can now be given by

$$u^{\text{L,min}}_{j+1/2} = \max\left[\min(u_j, u_{j+1}, u^{\text{MD}}_{j+1/2}), \min(u_j, u^{\text{UL}}_{j+1/2}, u^{\text{LC}}_{j+1/2})\right] \tag{3.10}$$

$$u^{\text{L,max}}_{j+1/2} = \min\left[\max(u_j, u_{j+1}, u^{\text{MD}}_{j+1/2}), \max(u_j, u^{\text{UL}}_{j+1/2}, u^{\text{LC}}_{j+1/2})\right]. \tag{3.11}$$

The monotonicity preserving value for $u^{\text{L}}_{j+1/2}$ can now be obtained by using the equation

$$u^{\text{L}}_{j+1/2} = \text{median}\left(u^{\text{L}}_{j+1/2}, u^{\text{L,min}}_{j+1/2}, u^{\text{L,max}}_{j+1/2}\right). \tag{3.12}$$

IV. NUMERICAL VERIFICATION OF THE HIGH-ORDER ACCURACY OF MPWENO SCHEMES

In this section we study numerically how the MPWENO schemes fare when it comes to achieving their designed accuracy. In the first subsection we study one-dimensional scalar problems. In the second subsection we study multidimensional problems, both scalar and systems of equations.

IV.a. *One Dimensional Problems*

Table IV shows several convergence studies for the advection equation, $u_t + u_x = 0$, with initial conditions $u_0(x) = \sin(\pi x)$, defined on $[-1, 1]$ with periodic boundary conditions.

TABLE IV

Method	Number of zones	L_1 error	L_1 order	L_∞ error	L_∞ order
$r = 5$	10	3.5827E-04		5.5930E-04	
WENO	20	6.1123E-07	9.20	1.1927E-06	8.87
	40	9.7166E-10	9.30	2.2653E-09	9.04
	80	1.6306E-12	9.22	4.1460E-12	9.09
$r = 5$	10	4.8003E-04		8.6886E-04	
MPWENO	20	6.1123E-07	9.62	1.1927E-06	9.51
$d_{j+1/2}^{\mathrm{MD}} = d_{j+1/2}^{\mathrm{M4X}}$	40	9.7166E-10	9.30	2.2653E-09	9.04
$d_{j+1/2}^{\mathrm{LC}} = d_{j+1/2}^{\mathrm{M4X}}$	80	1.6306E-12	9.22	4.1460E-12	9.09
$r = 3$	10	1.6694E-02		3.0224E-02	
MPWENO	20	7.5962E-04	4.46	1.4569E-03	4.37
$d_{j+1/2}^{\mathrm{MD}} = d_{j+1/2}^{\mathrm{M4X}}$	40	2.2698E-05	5.06	4.5939E-05	4.99
$d_{j+1/2}^{\mathrm{LC}} = d_{j+1/2}^{\mathrm{M4X}}$	80	6.9830E-07	5.02	1.4783E-06	4.96

The error was measured at $t = 1$. For this linear problem, LF, LLF, and RF building blocks all become the same. We used linear Runge–Kutta methods of the same order as the spatial operators with a CFL number 0.8.

The initial conditions for this problem are very smooth. We see that the $r = 5$ WENO scheme reaches its designed accuracy very rapidly and with a very small number of zones. In Table IV we also show results from $r = 5$ MPWENO with the most restrictive monotonicity preserving bounds given by $d_{j+1/2}^{\mathrm{MD}} = d_{j+1/2}^{\mathrm{LC}} = d_{j+1/2}^{\mathrm{M4X}}$. The $r = 5$ MPWENO scheme converges at the same rate and has almost the same errors as the $r = 5$ WENO scheme when 20 or more zones are used. This shows that the monotonicity restriction operator is having no effect in this case. This is a very desirable feature and it is also significant that it can be demonstrated for schemes with an order of accuracy as high as nine here. To enable us to compare and contrast with a lower-order scheme we also show the convergence study for $r = 3$ MPWENO with $d_{j+1/2}^{\mathrm{MD}} = d_{j+1/2}^{\mathrm{LC}} = d_{j+1/2}^{\mathrm{M4X}}$. Two very interesting insights can be gained from Table IV. First, we see that for small numbers of zones the higher-order scheme has a considerably smaller error than the lower-order scheme. Thus when the problem is not well resolved on a given computational grid the higher-order scheme nevertheless gives us a substantially smaller error than the lower-order scheme. Second, we see that when the problem is well resolved the substantially better convergence rate of the higher-order scheme allows it to obtain a significantly smaller error than the lower-order scheme. We have also carried out similar convergence studies for MPWENO schemes with $r = 4$, 6, and 7, and the general trends noted here for $r = 5$ MPWENO are repeated for these other schemes.

We have also performed a similar convergence study with the initial conditions $u_0(x) = \exp(\sin(\pi x))$ and found that it produces the same trends that were reported above for the $u_0(x) = \sin(\pi x)$ initial condition. For this reason, we do not tabulate that convergence study here.

Table V shows several convergence studies for the advection equation, $u_t + u_x = 0$, with initial conditions $u_0(x) = \sin^4(\pi x)$. It is important to point out that the initial conditions used here are very flat at each of the two maxima; that is, the first three derivatives are zero there. For this reason, Rogerson and Meiburg [32] found that the unbiased ENO schemes performed poorly for this problem. We see that the $r = 5$ WENO scheme in Table V suffers

TABLE V

Method	Number of zones	L_1 error	L_1 order	L_∞ error	L_∞ order
$r=5$	40	2.7674E-04		1.0711E-03	
WENO	80	9.1766E-07	8.24	7.4607E-06	7.17
	160	2.2566E-09	8.67	2.8738E-08	8.02
	320	6.5289E-12	8.43	1.2815E-10	7.81
$r=5$	40	4.8962E-04		2.4370E-03	
MPWENO	80	1.9091E-05	4.68	1.7941E-04	3.76
$d_{j+1/2}^{MD}=d_{j+1/2}^{MM}$	160	1.2575E-06	3.92	2.1792E-05	3.04
$d_{j+1/2}^{LC}=d_{j+1/2}^{MM}$	320	5.9172E-08	4.41	1.8768E-06	3.54
$r=5$	40	7.2627E-04		2.3674E-03	
MPWENO	80	4.0853E-05	4.15	2.7778E-04	3.09
$d_{j+1/2}^{MD}=d_{j+1/2}^{M4X}$	160	2.2955E-06	4.15	2.5640E-05	3.44
$d_{j+1/2}^{LC}=d_{j+1/2}^{M4X}$	160	1.3622E-07	4.07	2.8514E-06	3.17
$r=3$	40	3.6564E-03		8.9043E-03	
MPWENO	80	5.0389E-04	2.86	1.8086E-03	2.30
$d_{j+1/2}^{MD}=d_{j+1/2}^{MM}$	160	2.8389E-05	4.15	1.7678E-04	3.35
$d_{j+1/2}^{LC}=d_{j+1/2}^{MM}$	320	1.4393E-06	4.30	1.6388E-05	3.43

less from this problem, almost reaching its designed convergence rate at about 80 points. In Table V we also show the results from $r=5$ MPWENO schemes with the least restrictive monotonicity preserving bounds given by $d_{j+1/2}^{MD}=d_{j+1/2}^{LC}=d_{j+1/2}^{MM}$ and the most restrictive monotonicity preserving bounds given by $d_{j+1/2}^{MD}=d_{j+1/2}^{LC}=d_{j+1/2}^{M4X}$. This allows us to see the effect of imposing different kinds of monotonicity preserving bounds. We see clearly that even the imposition of the least restrictive monotonicity preserving bounds strongly degrades the order of accuracy of the scheme for this problem. An inspection of the time history of the buildup of the error shows that much of the error builds up very rapidly, i.e., within a time of 0.1 or less. We therefore see that the monotonicity preserving bounds do not live up to the full extent of the claim made in Suresh and Huynh [45] that they do not damage the order property of smooth solutions at all. The convergence rates in Table V show that they do, however, permit the scheme to achieve a fairly high order of accuracy. This serves to distinguish them from the older TVD limiters. By comparing the effect of the least and most restrictive monotonicity preserving bounds on the convergence rate in Table V we conclude that the effect of changing the monotonicity preserving bounds on the error or its convergence rate is not very significant. This leads us to the rather satisfying conclusion that most such monotonicity preserving bounds act similarly when imposed on MPWENO schemes with $r=5$. This conclusion is also verified numerically for MPWENO schemes with other values of r. Table V also permits us to compare $r=3$ MPWENO with $r=5$ MPWENO when both use $d_{j+1/2}^{MD}=d_{j+1/2}^{LC}=d_{j+1/2}^{MM}$. We see that the convergence rates for both schemes are determined by the fact that the monotonicity preserving constraints are used. However, we observe that the $r=5$ MPWENO scheme has errors that are almost an order of magnitude smaller than those of the $r=3$ MPWENO scheme when both schemes use the same number of grid points. Thus it indeed proves quite beneficial to go from an $r=3$ MPWENO scheme to an $r=5$ MPWENO scheme. This trend, however, does not extend to $r=6$ and $r=7$ MPWENO schemes, which have errors that are comparable to those of the $r=5$ MPWENO scheme for this test problem. This is an indication that for such

TABLE VI

Method	Number of zones	L_1 error	L_1 order	L_∞ error	L_∞ order
$r = 5$	20	1.1313E-03		8.4858E-03	
MPWENO	40	6.9382E-06	7.35	7.6824E-05	6.79
$d^{MD}_{j+1/2} = d^{M4}_{j+1/2}$	80	2.7680E-08	7.97	4.6426E-07	7.37
$d^{LC}_{j+1/2} = d^{M4}_{j+1/2}$	160	7.5166E-11	8.52	1.2535E-09	8.53

type of problems the $r = 5$ MPWENO is an optimal scheme and it may not be beneficial to use MPWENO schemes with $r > 5$.

Table VI shows a convergence study for the Burgers equation, $u_t + (u^2/2)_x = 0$, with initial conditions $u_0(x) = 0.25 + 0.5 \sin(\pi x)$. We used a third-order-accurate Runge–Kutta time-stepping strategy for this nonlinear problem as well as for the nonlinear 2D Euler equations in the next section. To hold down the errors from temporal discretiza-tion the time step Δt on successively refined grids was made to vary with the zone size Δx as $\Delta t \propto (\Delta x)^{(2r-1)/3}$. We carry out a convergence study for $r = 5$ MPWENO with $d^{MD}_{j+1/2} = d^{LC}_{j+1/2} = d^{M4}_{j+1/2}$ at a time of $1/\pi$, before the shock forms. We use the LLF flux here. Table VI shows clearly that the scheme is operating close to its designed accuracy. The trends shown in Table VI for $r = 5$ MPWENO also extend to MPWENO with $r = 4, 6,$ and 7.

The results from Tables IV and VI taken together allow us to conclude that the MPWENO schemes achieve their designed accuracy in one dimension for both linear and nonlinear hyperbolic equations when the solution is smooth and does not have a very flat extremum. When the solution does have a flat extremum the MPWENO schemes do show a degradation of their order property, as shown in Table V. The order of accuracy of the MPWENO schemes nevertheless remains quite high, especially when compared to the older TVD schemes. In such situations the $r = 5$ MPWENO scheme seems to be an optimal scheme when compared with the other higher-order schemes designed in this paper.

IV.b. *Multidimensional Problems*

Table VII shows several convergence studies for the two-dimensional advection equation, $u_t + u_x + u_y = 0$, with initial condition $u_0(x) = \sin^4(\pi x) \sin^4(\pi y)$. The problem was run on the area $[-1, 1] \times [-1, 1]$ with periodic boundaries and the result at $t = 1$ is shown. We show

TABLE VII

Method	Number of zones	L_1 error	L_1 order	L_∞ error	L_∞ order
$r = 5$	40×40	2.0434E-04		1.1146E-03	
WENO	80×80	6.7552E-07	8.24	7.5314E-06	7.21
	160×160	1.6650E-09	8.66	2.8819E-08	8.03
	320×320	4.8120E-12	8.43	1.2817E-10	7.81
$r = 5$	40×40	5.3034E-04		2.3487E-03	
MPWENO	80×80	3.0493E-05	4.12	2.7559E-04	3.09
$d^{MD}_{j+1/2} = d^{M4X}_{j+1/2}$	160×160	1.7532E-06	4.12	2.6314E-05	3.39
$d^{LC}_{j+1/2} = d^{M4X}_{j+1/2}$	320×320	1.0509E-07	4.06	2.9132E-06	3.18

the $r = 5$ WENO scheme and cross compare it with the $r = 5$ MPWENO scheme with the most restrictive monotonicity preserving bounds given by $d_{j+1/2}^{MD} = d_{j+1/2}^{LC} = d_{j+1/2}^{M4X}$. The results are very similar to those of the one-dimensional case shown in Table V, indicating that our schemes are as accurate in 2D as in 1D.

Porter *et al.* [30] have shown through DNS simulations that the evolution of compressible hydrodynamic turbulence is dominated by the evolution of structures of high vorticity once the initial phase of shock-dominated dissipation is over. To pick a test problem that is quite close to the target applications for the schemes designed here, we analyze the propagation of a strong vortex at a supersonic Mach number. The vortex propagates at $45°$ to the grid lines, which gives ample opportunity for the effects of multidimensional propagation to manifest themselves in this test problem. The problem is initialized on the two-dimensional domain given by $[-5, 5] \times [-5, 5]$. An unperturbed flow of the Euler equations with $(\rho, P, v_x, v_y) = (1, 1, 1, 1)$ and a ratio of specific heats given by $\gamma = 1.4$ is initialized on the computational domain. The temperature and entropy are defined as $T = P/\rho$ and $S = P/\rho^\gamma$. The vortex is defined as a fluctuation to this mean flow given by

$$(\delta v_x, \delta v_y) = \frac{\varepsilon}{2\pi} e^{0.5(1-r^2)}(-y, x)$$

$$\delta T = -\frac{(\gamma - 1)\varepsilon^2}{8\gamma \pi^2} e^{(1-r^2)}; \qquad \delta S = 0,$$

(4.1)

where $r^2 = x^2 + y^2$ and the vortex strength $\varepsilon = 5$. We utilize periodic boundary conditions.

In Table VIII we show the errors from the $r = 5$ MPWENO with $d_{j+1/2}^{MD} = d_{j+1/2}^{LC} = d_{j+1/2}^{M4}$ at a time of 10.0. By this time the vortex has travelled the entire length of the diagonal of the computational domain and is centered back again at the origin. We also show the results from $r = 3$ WENO. For both the $r = 5$ MPWENO and $r = 3$ WENO calculations we used a third-order-accurate Runge–Kutta scheme for the temporal. In order to help the reader to appreciate the effects of dimensional sweeping on higher-order Godunov schemes we also show the results of this same test problem run with the PPMDE variant of the PPM scheme in Colella and Woodward [13]. The results are shown for the PPM scheme run without either the PPM steepener or the PPM flattener. Another set of runs was carried

TABLE VIII

Method	Number of zones	L_1 error	L_1 order	L_∞ error	L_∞ order
$r = 5$	25×25	1.3518E-02		1.4072E-01	
MPWENO	50×50	1.9875E-04	6.09	4.6708E-03	4.91
$d_{j+1/2}^{MD} = d_{j+1/2}^{M4}$	75×75	3.7569E-05	4.11	1.4146E-03	2.95
$d_{j+1/2}^{LC} = d_{j+1/2}^{M4}$	100×100	1.0725E-05	4.36	4.1951E-04	4.23
$r = 3$	25×25	5.6303E-02		8.1172E-01	
WENO	50×50	4.8654E-03	3.53	8.3836E-02	3.28
	75×75	9.0182E-04	4.16	1.7957E-02	3.80
	100×100	2.4801E-04	4.49	5.9807E-03	3.82
PPM	25×25	4.4533E-02		7.5762E-01	
	50×50	1.2806E-02	1.80	1.6085E-01	2.24
	75×75	7.7270E-03	1.25	8.5558E-02	1.56
	100×100	3.7955E-03	2.47	5.0517E-02	1.83

out with the PPM steepener and the results were found to be almost identical to those shown in Table VIII. Symmetrized interleaving of sweeps in the x- and y-directions were used for the temporal update of the PPM scheme. This directional splitting of the Euler equations was proposed by Strang [44] and is expected to result in a temporal update that is second-order accurate in space and time. In the previous subsection we showed that the CFL number needs to be decreased with increasing mesh resolution in order to enable the scheme to reach its design accuracy. Most realistic simulations are done at a finite CFL number that is held fixed as the resolution of the simulation is increased. It is also computationally impracticable to do a convergence study in multiple dimensions with a CFL number that decreases with increasing resolution. For both these reasons we have run the WENO and MPWENO convergence studies with a fixed CFL number of 0.2. For the PPMDE calculations we used a CFL number of 0.2 for each individual sweep. We see from Table VIII that the $r = 5$ MPWENO scheme is the most accurate scheme among the schemes considered. If a fixed resolution is to be used, the $r = 5$ MPWENO is at least an order of magnitude more accurate than the $r = 3$ WENO scheme. At fixed resolution, both schemes are substantially more accurate than the PPMDE scheme. We see from Table VIII that the $r = 5$ MPWENO can obtain about the same accuracy on a grid of 50×50 zones that the $r = 3$ WENO achieves on a grid of 100×100 zones. We also see that even on a grid of 100×100 zones the PPM scheme only produces a solution with accuracy that is roughly comparable with the $r = 3$ WENO scheme's accuracy on a grid of 50×50 zones.

Further insight can be gained by paying attention to the quantitative values in Table VIII. Ghosal [15] has shown that the subgrid force terms in the typical situations considered by him are not much larger than 10% of the total force terms. THus being able to model the subgrid force terms in an LES calculation with a nominal 10% accuracy requires that one be able to simulate features in the flow with at least 1% accuracy. For this problem the density, vortex velocity, and radius of the vortex are all of the order of unity, implying that the total force is of the order of unity in the vortex. We see that even when 25×25 zones are used the $r = 5$ MPWENO scheme has an error in the L_1 norm that is at the 1% level. The PPM scheme, on the other hand, achieves an error in the L_1 norm that is at the 1% level on a grid of 50×50 zones. To model the subgrid forces in an LES simulation one is more likely to be interested in the error measured in the L_∞ norm. The $r = 5$ MPWENO scheme achieves an error in the L_∞ norm that is better than 1% with a mere 50×50 zones. The PPM scheme does not achieve a comparable error in the L_∞ norm even on a 100×100 zone grid. This provides a quantitative demonstration of the claim made in Ghosal [15] that second-order schemes do not reduce the error fast enough on any of the scales represented in the computation to permit accurate LES sibgrid modeling to be done for the scales that are not represented in the computation.

V. ACM AND THE HIGHER-ORDER PROPERTIES OF MPWENO SCHEMES THAT USE ACM

When isolated discontinuities in linearly degenerate characteristic fields are present in the flow it is customary to want to improve their profile so as to endow them with as sharp a profile as possible. This is usually done by using the ACM strategy, where one adds an extra linear profile to the interpolant in a given zone. This profile is only added when the addition of such a profile does not destroy the TVD property. The addition of this linear

profile is intended to steepen the interpolated profile in the zone. There are two questions which must be addressed in this procedure: (1) What is the right amount of steepening to add to schemes of high order such as the ones designed here? (2) What are the consequences of the ACM on the order property of numerical schemes, especially the schemes with very high order of accuracy designed here? Yang [50] has designed an ACM scheme that has proven particularly popular. We seek to answer these two questions within the context of Yang's ACM.

As in Section III we focus on the interpolation of a scalar quantity u to the zone boundary $x_{j+1/2}$. The interpolated values on the left and right of the zone boundary are denoted by $u^L_{j+1/2}$ and $u^R_{j+1/2}$, respectively. These interpolated values are to be obtained by using the MPWENO interpolation strategy. Since the scheme designed here operates on characteristic variables the extension to hyperbolic systems can be trivially made by steepening the weights in Eq. (2.4) for any characteristic field that needs to be steepened using ACM. The slope modifier for the interpolated profile in zone j is then given by

$$\delta u_j = 2\text{minmod}\big[\sigma_j \, \text{minmod}\big(u^R_{j-1/2} - u^L_{j-1/2}, u^R_{j+1/2} - u^L_{j+1/2}\big),$$
$$\text{minmod}\big(u_{j+1} - u^L_{j+1/2}, u^R_{j-1/2} - u_{j-1}\big)\big] \tag{5.1}$$

so that the value of $u^L_{j+1/2}$ is modified as follows:

$$u^L_{j+1/2} \to u^L_{j+1/2} + \frac{1}{2}\delta u_j. \tag{5.2}$$

The coefficient of the slope modifier σ_j in Eq. (5.1) can be written as the product of a discontinuity detector μ_j and a balance factor ψ_j as

$$\sigma_j = c\mu_j\psi_j, \tag{5.3}$$

where we have

$$\mu_j = \left(\frac{u_{j+1} - 2u_j + u_{j-1}}{|u_{j+1} - u_j| + |u_j - u_{j-1}|}\right)^2 \tag{5.4}$$

and

$$\psi_j = \left|\frac{u_j - u_{j-1}}{u_{j+1} - u_j}\right|^{b((\lambda_j \Delta t/\Delta x) - 0.5\,\text{sgn}(\lambda_j))} \quad \text{when } (u_j - u_{j-1})(u_{j+1} - u_j) > 0$$
$$= 0 \quad \text{otherwise.} \tag{5.5}$$

The variable λ_j in Eq. (5.5) denotes the signal speed at which the variable u is being advected in zone j. For a hyperbolic system it refers to the characteristic speed of the characteristic field in zone j that is being treated by the ACM technique. Equations (5.3) and (5.5) show clearly that the variables c and b are variables whose values have to be set in the ACM. The variable b affects the way the scheme introduces a balance between ascending and descending profiles and needs to be set to 4.3 for all the schemes used here. The variable c may be set to different values for schemes of different orders and determines the amount of steepening introduced by the ACM. It needs to be set by trial and error.

TABLE IX

Method	Number of zones	L_1 error	L_1 order	L_∞ error	L_∞ order
$r = 5$, ACM,	10	4.6231E-04		8.1426E-04	
MPWENO	20	5.1904E-07	9.80	1.0259E-06	9.63
$d^{MD}_{j+1/2} = d^{M4X}_{j+1/2}$	40	2.3023E-09	7.82	7.8494E-09	7.03
$d^{LC}_{j+1/2} = d^{M4X}_{j+1/2}$	80	6.2205E-12	8.53	2.9266E-11	8.07

Through extensive trial and error we have found that when the variable c in Eq. (5.3) is given a large value and used in very high order schemes it actually damages the structure of discontinuities. Thus higher-order schemes need smaller values of c. Higher-order schemes can, however, capture discontinuities in linearly degenerate characteristic fields and propagate them without much degradation even when the ACM is not used. Hence with increasing order of accuracy there is a diminishing need to rely on the ACM. We have experimented with several hyperbolic systems including scalar advection, the Euler equations, and the equations of ideal MHD. The value of c to be used for optimal capturing of discontinuities belonging to linearly degenerate characteristic fields does not seem to depend sensitively on the particular hyperbolic system being solved when the order of the MPWENO scheme is held fixed. This is a very desirable result because it shows that the optimal value of c to be used does not vary from one hyperbolic system to another. Thus for $r = 3$ MPWENO we recommend that the maximal value of c be $c = 20.0$, though $c = 25$ is permissible on occasion. For $r = 4$ MPWENO the maximal value of c is given by $c = 20.0$. For $r = 5$ MPWENO we suggest using a maximal value of c given by $c = 15.0$, though $c = 20.0$ might sometimes be acceptable. For $r = 6$ MPWENO we suggest using $c = 15.0$ and for $r = 7$ MPWENO we recommend not using ACM at all. In general we find that MPWENO schemes with even values of r do not take as well to the use of ACM as MPWENO schemes with odd values of r. It is also worth pointing out that schemes with $r \geq 5$ can propagate discontinuities with about seven zones in them without any degradation in the discontinuity's profile and so do not necessarily need to rely on the use of steepening techniques such as ACM. We will show this numerically in the next section. To view this in a different way, in certain problems where very accurate propagation of discontinuities is strongly desired it may be more acceptable to allow discontinuities to propagate with a natural width of seven zones and high phase accuracy than to make them propagate with an artificially steepened width of three zones and risk a degradation in phase accuracy. The previous comment has special relevance to turbulence calculations, where very accurate propagation of flow structures has a great deal of bearing on the accuracy of the results.

In Table IX we show the convergence study for $r = 5$ MPWENO with $c = 20.0$ for the advection problem with initial conditions given by $u_0(x) = \sin(\pi x)$. By comparing the results in Table IX with the reuslts in Table IV we see clearly that the accuracy and the order of the scheme are not affected significantly by the use of ACM.

VI. ONE DIMENSIONAL TESTS

VI.a. *Scalar Advection*

Our first test problem consists of testing the behavior of the scheme on a rather stringent scalar advection test problem. This is the same test problem that was catalogued in Jiang

and Shu [23]. Thus we solve the problem

$$u_t + u_x = 0 \qquad -1 < x < 1$$

$$u(x, 0) = u_0(x) \qquad \text{periodic}$$

(6.1)

with

$$
\begin{aligned}
u_0(x) &= \frac{1}{6}[G(x, \beta, z - \delta) + G(x, \beta, z + \delta) + 4G(x, \beta, z)] & -0.8 \le x \le -0.6 \\
&= 1 & -0.4 \le x \le -0.2 \\
&= 1 - |10(x - 0.1)| & 0.0 \le x \le 0.2 \\
&= \frac{1}{6}[F(x, \alpha, a - \delta) + F(x, \alpha, a + \delta) + 4F(x, \alpha, a)] & 0.4 \le x \le 0.6 \\
&= 0 & \text{otherwise}
\end{aligned}
$$

(6.2)

$$G(x, \beta, z) = e^{-\beta(x-z)^2}$$

$$F(x, \alpha, a) = \sqrt{\max(1 - \alpha^2(x - a)^2, 0)}.$$

(6.3)

The constants in Eqs. (6.2) and (6.3) are given by

$$a = 0.5; \qquad z = -0.7; \qquad \delta = 0.005; \qquad \alpha = 10; \qquad \beta = \frac{\log 2}{36\delta^2}.$$

(6.4)

The problem has several shapes that are difficult to advect with fidelity. The shapes consist of: (1) a combination of Gaussians, (2) a square wave, (3) a sharply peaked triangle, and (4) a half-ellipse arranged initially from left to right. This is a stringent test problem because it has a combination of functions that are not smooth and functions that are smooth but sharply peaked. The Gaussians differ from the triangle in that the Gaussians' profile actually has an inflection in the second derivative. A good numerical method that can advect information with a high level of fidelity must be able to preserve the specific features of the problem that we have catalogued above. The problem was initialized on a mesh of 200 zones. It was run for a simulation time of 20, which corresponds to 10 traversals around the mesh. In doing so the features catalogued in Eqs. (6.2) and (6.3) were advected over 2000 mesh points. The problem was run with a CFL number of 0.4.

In Fig. 1a we show the results from $r = 5$ MPWENO with $d^{MD}_{j+1/2} = d^{LC}_{j+1/2} = d^{M4}_{j+1/2}$. In Fig. 1a the ACM steepener was not used. To aid comparison with the exact solution, the exact solution is also shown in the figure with a solid line. We see that the different shapes have been accurately advected so that one can readily pick out the differences between the different shapes even after 10 traversals around the computational mesh. The peaks in the Gaussians and the triangle have been preserved without any substantial flattening of the points at their maxima. The fact that the Gaussians have an inflection in the second derivative while the triangle does not can also be seen. The square pulse has retained its flat top. About seven points have been put in by the scheme to represent the rising and falling parts of the square pulse. This is the motivation for our claim in Section V that these very high order schemes can advect profiles well without smearing them over much more than seven zones.
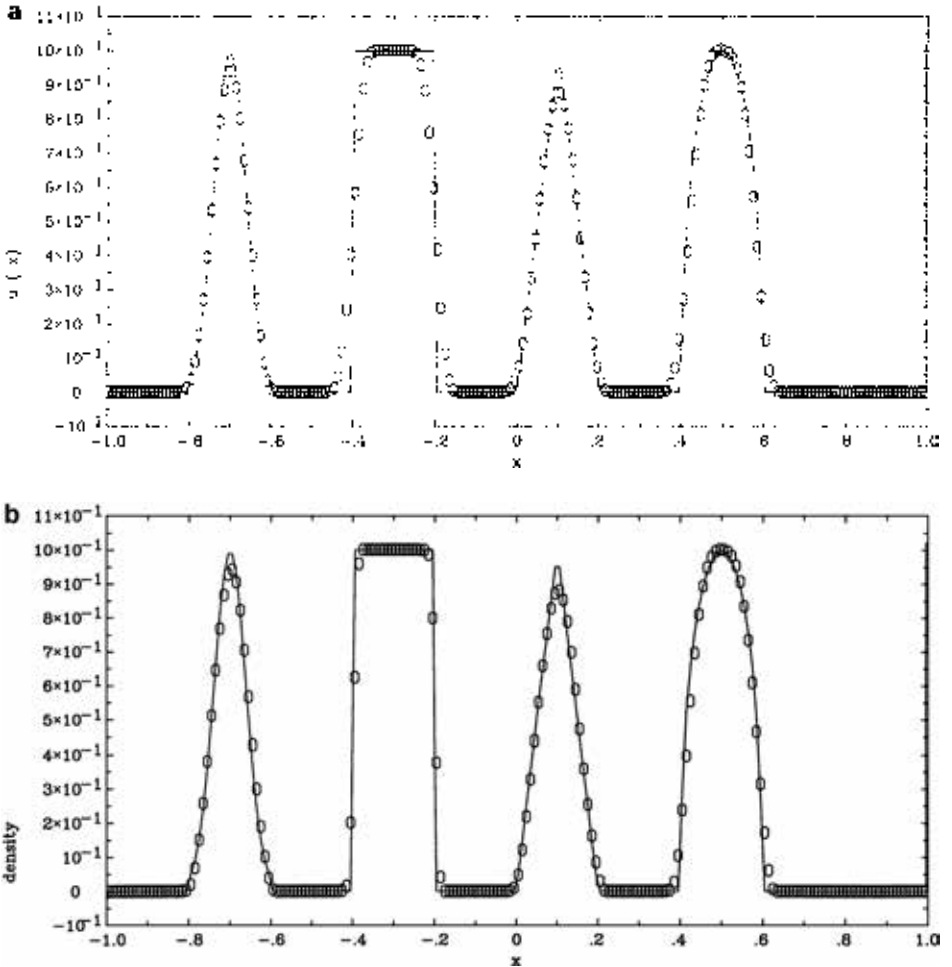
FIG. 1. The scalar advection test problem catalogued in Eqs. (6.2), (6.3), and (6.4). The iniitial profile was allowed to propagate 10 times around the computational domain with CFL number 0.4. (a) The result for $r = 5$ MPWENO without ACM. (b) The same as (a) but with ACM. (c) The result from the PPM scheme without the steepener. (d) The result from the PPM scheme with the steepener.

They are able to do this without needing to rely on the ACM steepener. The rounded top of the parabolic profile is accurately captured and stands out in contradistinction to the flattened top of the square wave. Notice, too, that the profiles of all the pulses are fully symmetrical about their peaks, which is a very desirable feature in a numerical algorithm. Figure 1b shows the same scheme with the ACM also being used. We used the same suggested values for the coefficients in the ACM steepener that we catalogued in Section V. We see that the square wave profile has become sharper. The other strongly peaked shapes have not been damaged. The parabolic profile has not had any numerically induced change in its curvature. We observe a slight asymmetrical aspect in the profiles in Fig. 1b when compared to those in Fig. 1a. But the balancing factor in Eq. (5.5) has ensured that the profiles are, for the most part, very symmetrical. Thus the ACM step has been mostly beneficial for the square wave pulse where it was most needed and unobtrusive for the elliptical wave pulse
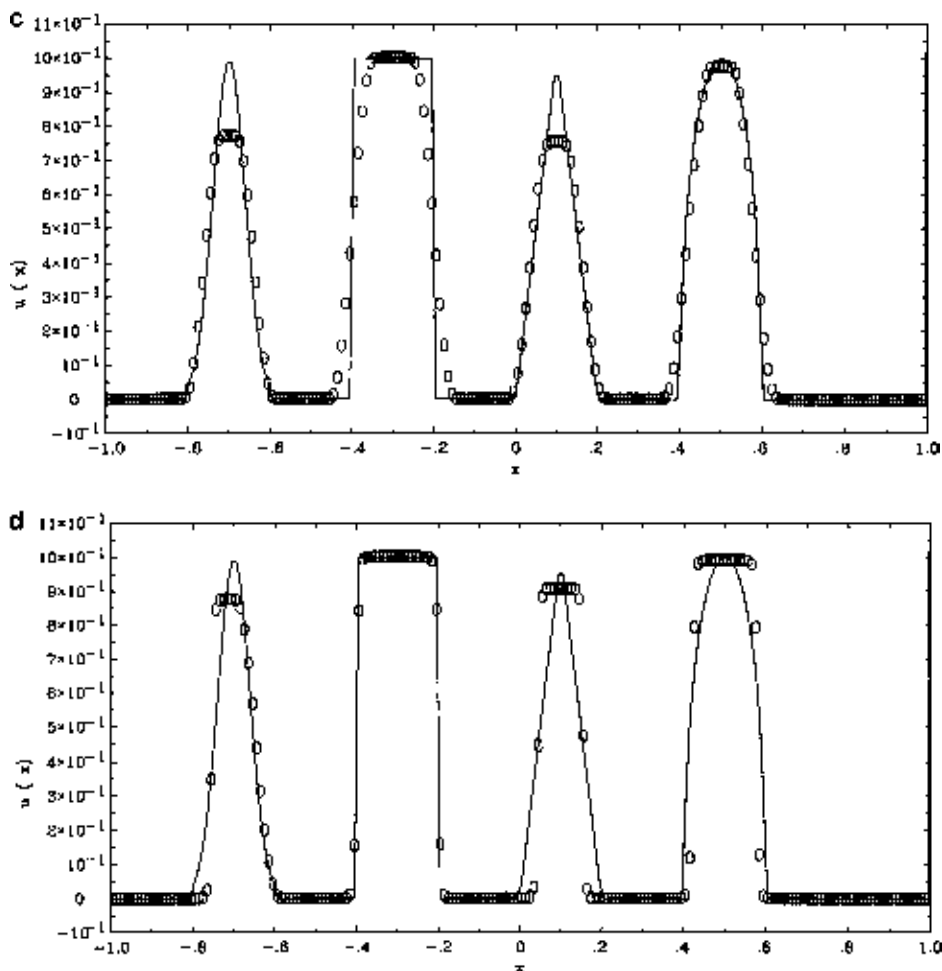
FIG. 1—*Continued*

where it was not needed. Thus Yang's ACM behaved very well on this rather stringent test problem.

In Figs. 1c and 1d we show the performance of the PPM method of Colella and Woodward [13] on this test problem. Figure 1c was produced by a run without the contact discontinuity steepener. Figure 1d was obtained from a run with the contact discontinuity steepener that is described in Colella and Woodward [13]. We used the Lagrange-remap version of PPM, which has a slightly higher accuracy than the direct-Eulerian version of PPM for this type of problem. Because piecewise parabolic profiles can be exactly integrated for the scalar advection equation, the test problem was done without any errors emanating from the temporal discretization. We used a CFL number of 0.4 as in the previous case. It is beneficial to be able to compare and contrast the performance of the higher-order schemes designed here with the traditional TVD schemes. We see from Fig. 1c that PPM has flattened the tops of all the pulses in the problem. This has resulted in considerable degradation of the Gaussians' profile and the triangle's profile. The rising and falling parts of the square wave have about eight to nine zones across them. We also see that the profiles of all the other pulses have the same number of zones in their rising and falling parts along with flat tops.

Thus the PPM scheme has effectively turned all the different pulse shapes into profiles that are equivalent to a square pulse. This indicates that the PPM scheme, because it is a TVD scheme and relies on TVD limiters, has suffered a genuine loss of phase accuracy. Figure 1d shows the effect of the steepener catalogued in Colella and Woodward [13]. We see that most of the pulses have been turned into square wave pulses with sharp edges. The leading edge of the Gaussians' pulse is asymmetrical when compared to its trailing edge. This is a clear consequence of the steepener in PPM not having a balancing factor like the ACM algorithm of Yang [50]. From Figs. 1c and 1d we see that all the phase accuracy has been lost in the solutions that were computed with the PPM algorithm.

VI.b. *Hydrodynamical Interacting Blast Wave Problem*

We have run the interacting blast wave problem from Woodward and Colella [49] using exactly the same parameters used by those authors. The problem was run with the $r = 5$ MPWENO scheme with $d_{j+1/2}^{MD} = d_{j+1/2}^{LC} = d_{j+1/2}^{M4}$. The RF version of the scheme was used. The ACM method was used with the parameters suggested in Section V for the $r = 5$ MPWENO scheme. A CFL number of 0.6 was used. In Fig. 2 we show the density variable from a 400-zone simulation with open circles. The solid line shows the converged density obtained from a 1000-zone simulation. We see that the left-going contact discontinuity is captured very well even in the 400 zone simulation. We also see that the density profile from the 400-zone simulation is very close to the converged density profile.
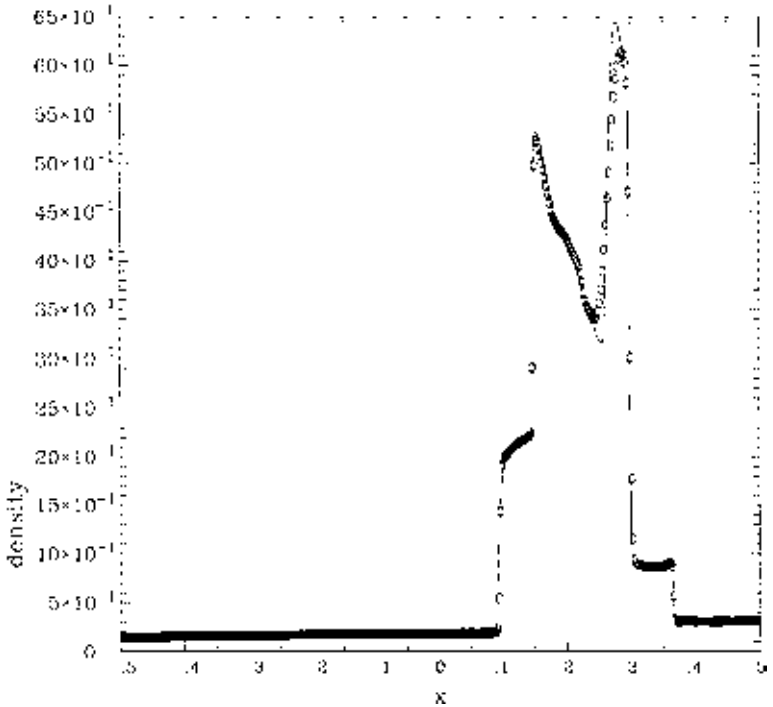
FIG. 2. The density profile at a time of 0.038 for the interacting blast waves problem. The $r = 6$ MPWENO scheme was used with ACM. The problem was run with a CFL number of 0.6. The open circles show the results of a 400-zone simulation. The solid line is a converged density profile obtained from a 1000-zone simulation.

It is also worth noting that we have run the classical shock tube test problems by Sod [43] and Lax [24] with the schemes designed here and obtained good results.

VI.c. *MHD Shock Tube Problems*

In order to illustrate the versatility of the methods developed here and their applicability to other hyperbolic systems we apply them to a couple of Riemann problems that are drawn from MHD. The eigenstructure of MHD has been thoroughly explored in Roe and Balsara [36], a linearized Riemann solver was developed in Balsara [1], and TVD schemes for MHD were developed in Balsara [2]. Balsara and Spicer [4] have constructed a divergence-free formulation of MHD. Because such formulations use both the zone-centered and the face-centered values of the magnetic field the MPWENO methodology has to be extended to accommodate such a staggering of variables. This extension, which is specific to numerical MHD, has been carried out by Balsara and will be reported by him in a later publication. For one-dimensional MHD problems this extension is unessential and the methods developed here are perfectly adequate for treating such problems. Therefore we report on a couple of one-dimensional MHD Riemann problems here. Both were run with the $r = 5$ MPWENO scheme with $d_{j+1/2}^{MD} = d_{j+1/2}^{LC} = d_{j+1/2}^{M4X}$. The RF version of the algorithm was used here. The ACM method was used with the parameters that are suggested in Section V for the $r = 5$ MPWENO scheme. The ACM was applied to all the linearly degenerate characteristic fields in the problem. A CFL number of 0.6 was used. For MHD it was found useful to set $\chi = 1.3$ in Eq. (2.5).

Figures 3a to 3e show the density, pressure, x-velocity, y-velocity, and y-component of the magnetic field, respectively, for the Brio–Wu [6] test problem. The problem is specified on a 400-zone mesh that covers the region $[-0.5, 0.5]$. The 400 mesh points are shown as open circles. The solid line corresponds to the exact solution. The initial conditions are given by

$$(\rho_L, P_L, v_{x,L}, v_{y,L}, v_{z,L}, B_{y,L}, B_{z,L}) = (1, 1, 0, 0, 0, 1.0(4\pi)^{1/2}, 0.0) \qquad x < 0$$

$$(\rho_R, P_R, v_{x,R}, v_{y,R}, v_{z,R}, B_{y,R}, B_{z,R}) = (0.125, 0.1, 0, 0, 0, -1.0(4\pi)^{1/2}, 0.0) \qquad x > 0$$

$$B_x = 0.75(4\pi)^{1/2}.$$

$$(6.5)$$

The problem was run up to a simulation time of 0.1. The ratio of specific heats was set to 2.0. The ACM was used in Figs. 3a to 3e. Figure 3f shows the density from the same test problem when the ACM was not used. The problem generates a right-going fast rarefaction wave, a right-going slow shock, a contact discontinuity, a left-going slow compound wave, and a left-going fast rarefaction wave. Alfven waves are not generated since the problem is coplanar. We see that all the shocks are captured with sharp, oscillation-free profiles. The contact discontinuity is also represented with a sharp profile having just a few zones across it. We see that the representation of the contact discontinuity without ACM is almost as good as its representation with ACM. This bears out the claim we made in Section V that these very high order schemes do not need to rely much on ACM-type steepening techniques to achieve good representation of linearly degenerate characteristic fields. It is significant that this claim is as true for the MHD equations, which have a richer wave structure, as it is for the Euler equations. We conclude from the above discussion that the $r = 5$ MPWENO scheme has been able to capture all the features in the problem very well. Because this is
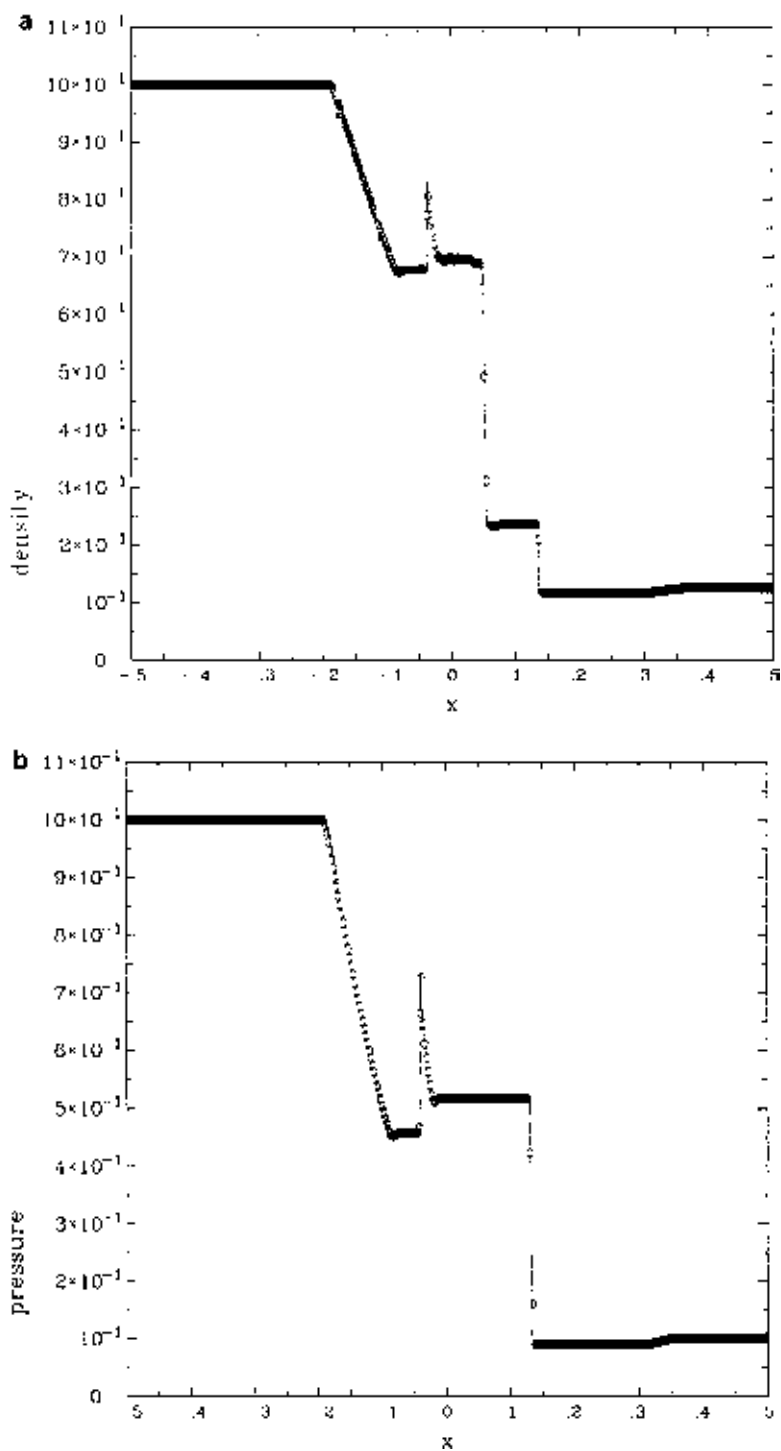
FIG. 3. (a)–(e) The density, pressure, x-velocity, y-velocity, and y-component of the magnetic field, respectively, for the Brio–Wu [6] test problem. It was run to a time of 0.1. In either case the $r = 5$ MPWENO scheme was used with ACM. The problem was run with a CFL number of 0.6. (f) The density for the same test problem when the ACM was not used. The 400 mesh points used in this problem are shown as open circles. The solid line corresponds to the exact solution.
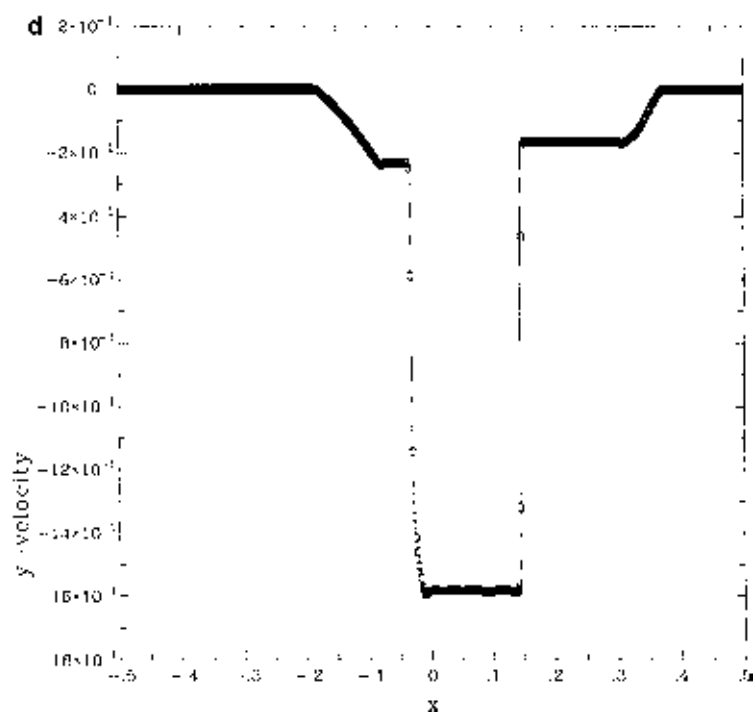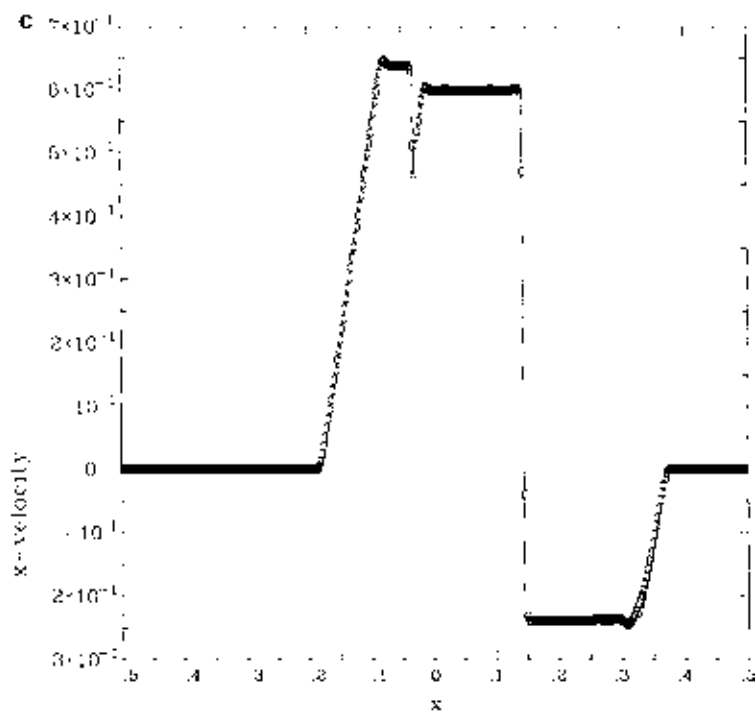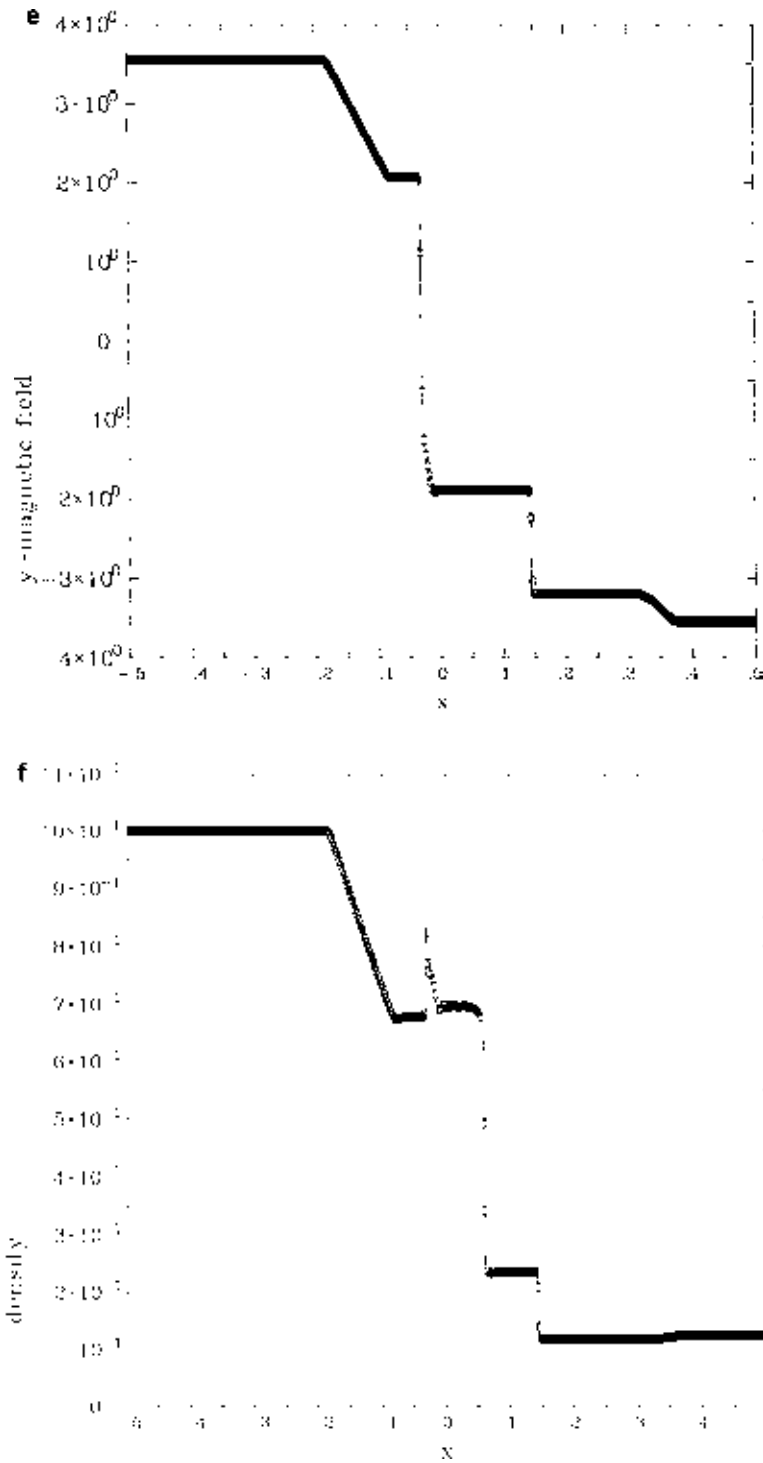
FIG. 3—*Continued*

FIG. 3—*Continued*

a very high order scheme it was able to achieve very good definition of the features in the flow by using a computational grid with just 400 zones.

Figures 4a to 4g show the density, pressure, x-velocity, y-velocity, z-velocity, and y-component, and z-component of the magnetic field, respectively, for one of the test problems in Ryu and Jones [37]. The problem is specified on a 400-zone mesh that covers the region $[-0.5, 0.5]$. The 400 mesh points are shown as open circles. The solid line corresponds to the exact solution. The initial conditions are given by

$$(\rho_L, P_L, v_{x,L}, v_{y,L}, v_{z,L}, B_{y,L}, B_{z,L}) = (1.08, 0.95, 1.2, 0.01, 0.5, 3.6, 2.0) \qquad x < 0$$
$$(\rho_R, P_R, v_{x,R}, v_{y,R}, v_{z,R}, B_{y,R}, B_{z,R}) = (1.0, 1.0, 0, 0, 0, 4.0, 2.0) \qquad x > 0$$
$$B_x = 2.0$$

$$(6.6)$$

This was run to a simulation time of 0.2. The ratio of specific heats was set to 5/3. Figures 4a to 4g show the results when ACM was used. Figures 4h and 4i show the density and y-component of the magnetic field in the same problem when ACM was not used. This is a non-coplanar problem. It, therefore, generates seven waves, the waves being a right-going fast shock, a right-going rotational discontinuity, a right-going slow shock, a contact discontinuity, a left-going slow shock, a left-going rotational discontinuity, and a left-going fast shock. We see that all the shocks are properly captured with only a few zones across the shock profile. It is also significant that this very high order scheme captures slow shocks with just a few zones. It was found in the study of TVD schemes for MHD—see Balsara [2]—that the profiles of slow shocks sometimes have a few more zones across them than might be deemed optimal. This trend is exacerbated when one studies TVD schemes for relativistic MHD; see Balsara [4]. By observing Fig. 4 we notice that the $r = 5$ MPWENO scheme represents slow shocks with a crisp profile. Thus using the very high order schemes designed here improves the representation of slow magnetosonic shocks. We also notice from Fig. 4 that the contact discontinuity and the rotational discontinuities are captured properly with just a few zones across their profiles. This is as true when the ACM algorithm is used as when it is not used, showing once again that the very high order schemes designed here do not need to rely much on ACM-type steepeners. From Figs. 4e and 4f we see that there are only a few zones between the rotational discontinuities and the corresponding slow shocks. The ability of the scheme to represent all discontinuities with sharp profiles is vital for keeping the rotational discontinuities distinct from the slow shocks and representing their profiles with a high degree of accuracy. This has allowed us to carry out the present simulation on a grid of 400 zones. To obtain a comparable quality in the solution from a TVD scheme would have required doing the problem on a grid of 800 zones. This illustrates the considerable advantages of the very high order MPWENO schemes designed here.

VI.d. *Shock–Entropy Wave Interaction*

In Section IV, where we did a fair bit of convergence testing, we showed that it was advantageous to go to higher order. It is interesting to ask whether these advantages are realized in a realistic test problem. Shu and Osher [39] presented a problem where a Mach 3 shock wave interacts with a density disturbance and generates a flow field that has a combination of smooth structures and discontinuities. This problem is a good model for the kinds of interactions that occur in simulations of compressible turbulence. It represents
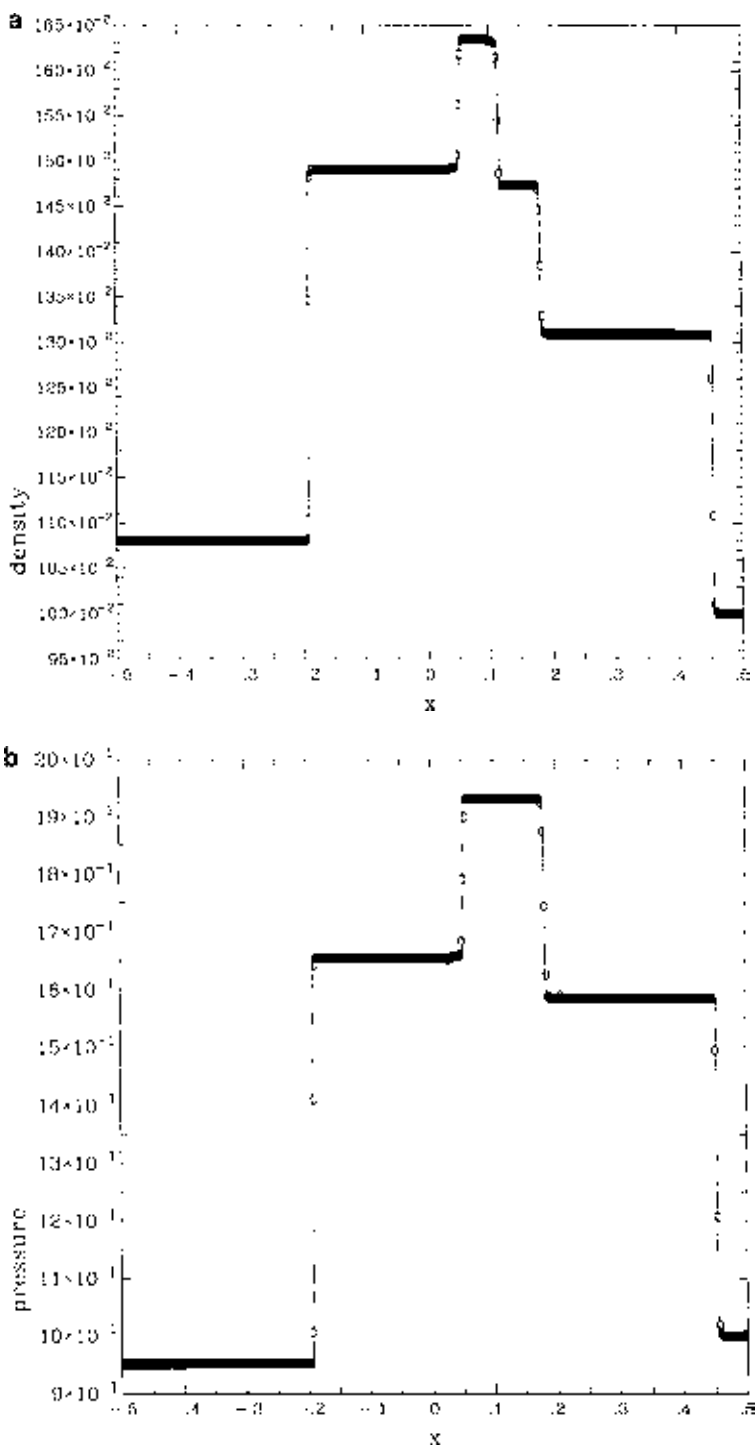
FIG. 4. (a)–(g) The density, pressure, x-velocity, y-velocity, z-velocity, y-component, and z-component of the magnetic field, respectively, for one of the test problems in Ryu and Jones [37]. It was run to a time of 0.2. In either case the $r = 5$ MPWENO scheme was used with ACM. The problem was run with a CFL number of 0.6. (h) and (i) The density and y-component of the magnetic field for the same test problem when the ACM was not used. The 400 mesh points used in this problem are shown as open circles. The solid line corresponds to the exact solution.
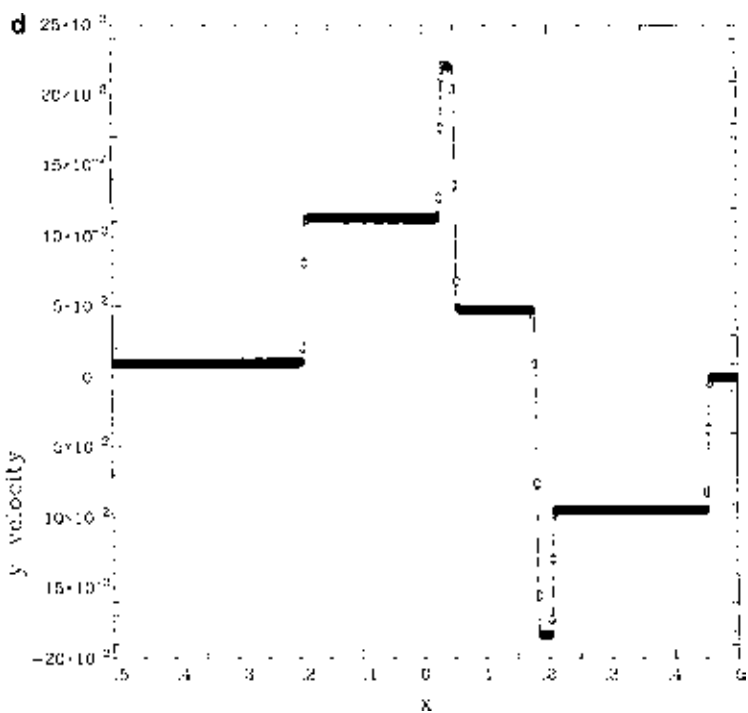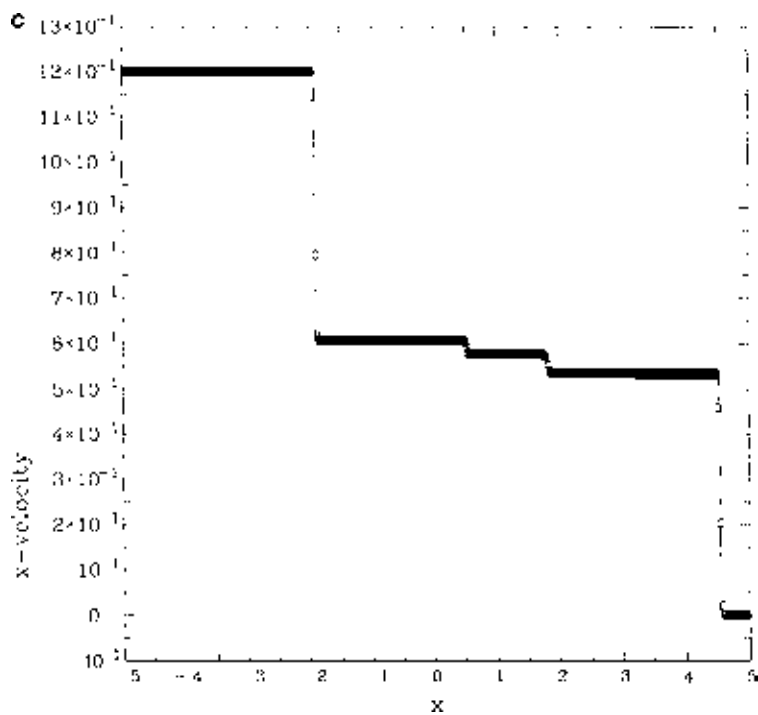
FIG. 4—*Continued*
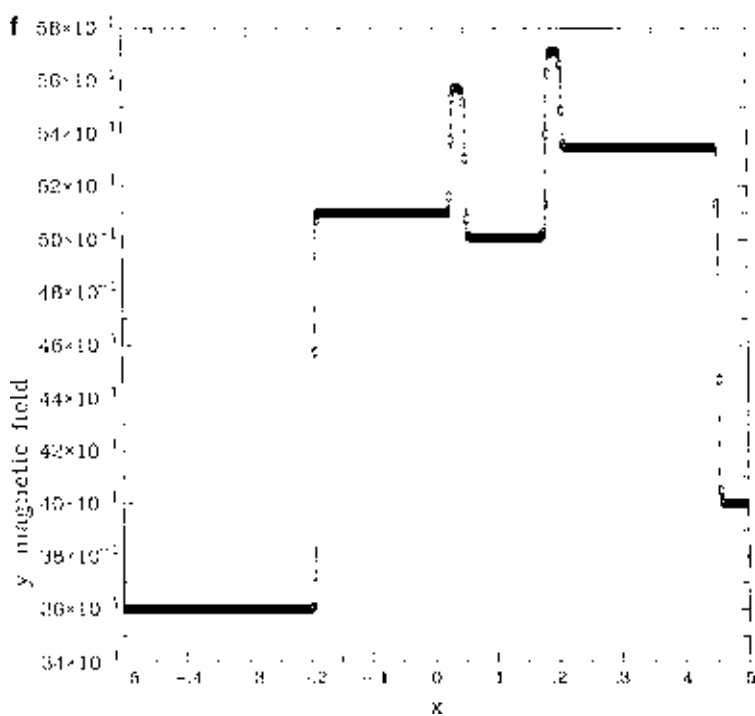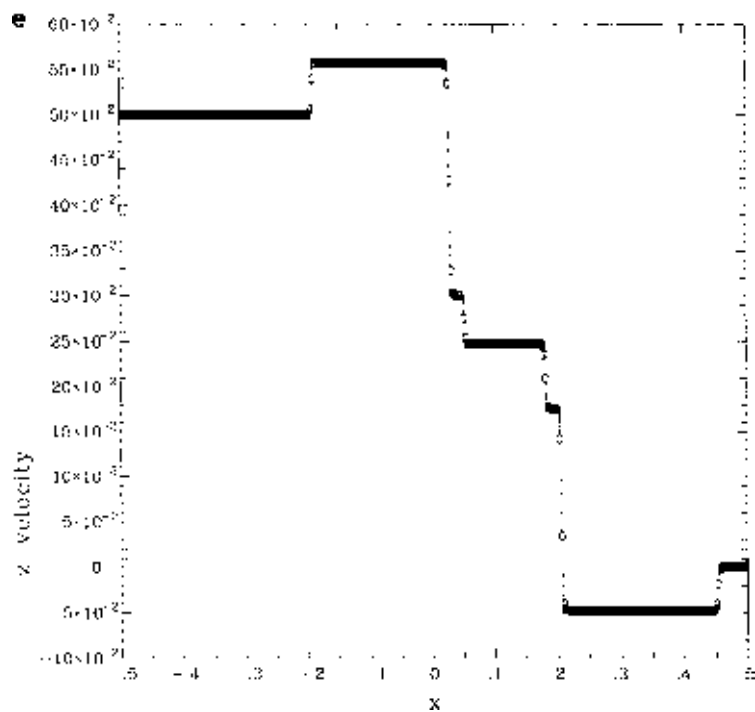
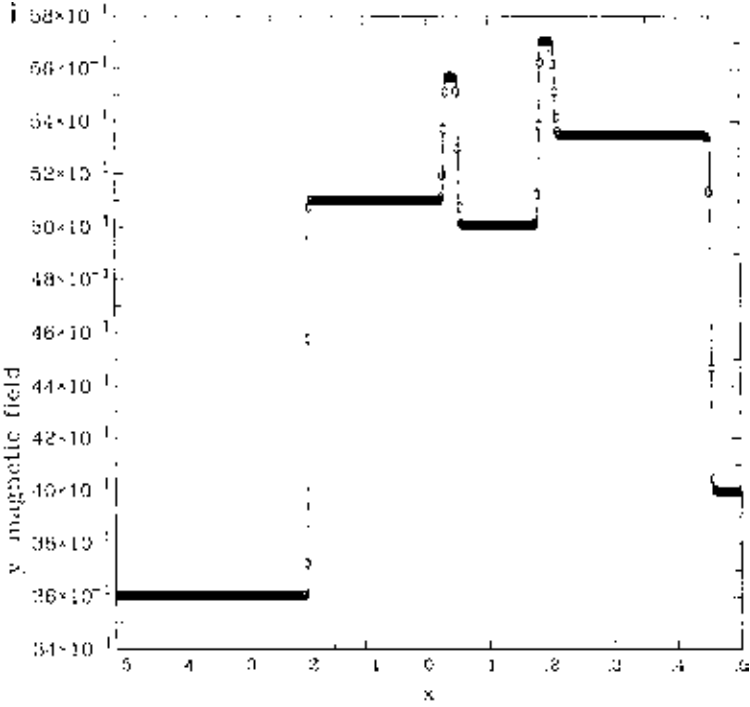FIG. 4—*Continued*
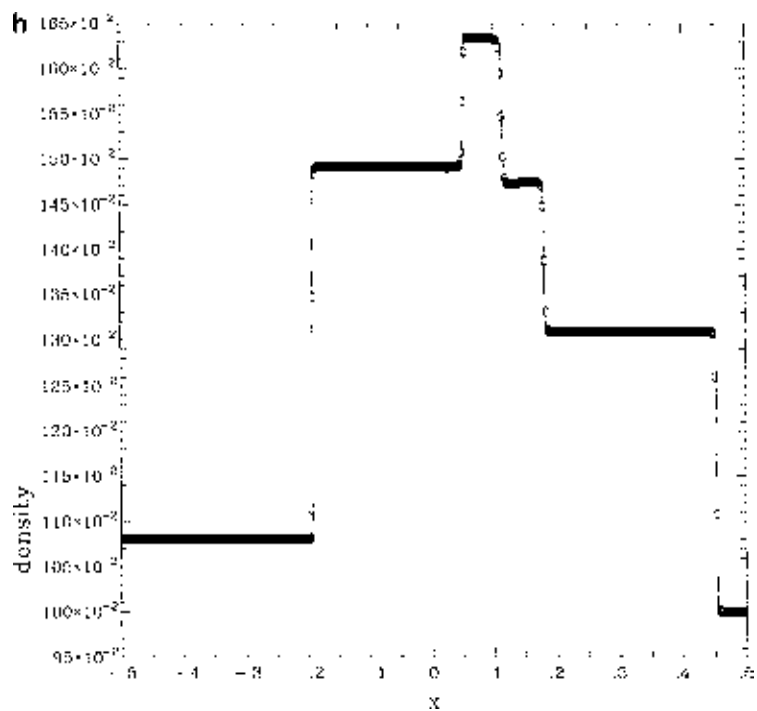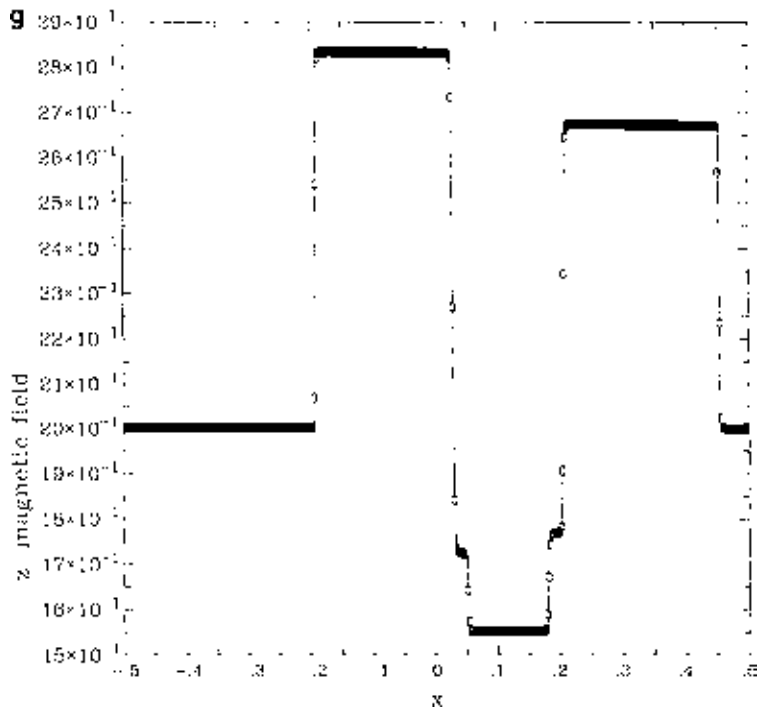
FIG. 4—*Continued*

FIG. 4—*Continued*

the amplification of entropy fluctuations as they pass through a strong shock. As mentioned in the Introduction, accurate capturing of isolated discontinuities, such as shocks, does not pose a problem for second-order-accurate TVD schemes. It is the interaction of smooth structures with shocks that poses a problem because that is where the damaging effects of TVD limiters are maximal. Jiang and Shu [23] have carried out a detailed comparative study showing that the performance of the $r = 3$ WENO scheme is far superior to that of a well-designed TVD scheme. Jiang and Shu [23] came to the important conclusion that the $r = 3$ WENO scheme with 800 zones outperformed the TVD scheme with 2000 zones by a substantial margin. To examine the role of increasing order of accuracy we make a comparison between the $r = 3$ WENO scheme and the $r = 5$ MPWENO scheme designed here. The $r = 5$ MPWENO scheme was run with $d_{j+1/2}^{MD} = d_{j+1/2}^{LC} = d_{j+1/2}^{M4}$. Both schemes were run with a CFL number of 0.6. The RF version of the numerical flux was used for both schemes. We did not use the ACM for either of the schemes. The problem was run on a grid of 200 zones in the interval $[-1, 1]$. The initial conditions are specified by

$$
\begin{aligned}
(\rho_L, P_L, v_{x,L}) &= (3.857143, 10.3333, 2.629369) & x &< -0.8 \\
(\rho_R, P_R, v_{x,R}) &= (1 + 0.2\ \sin(5\pi x), 1, 0) & x &> -0.8.
\end{aligned}
\tag{6.7}
$$

The problem was run upto a simulation time of 0.47.

The points in Fig. 5a show the density from the $r = 5$ MPWENO scheme run on a grid with 200 zones. We also ran the $r = 5$ MPWENO scheme on a grid of 800 zones in order to generate a reference calculation. The density from the reference calculation is shown as the solid line in Fig. 5a. The points in Fig. 5b show the density from the $r = 3$ WENO
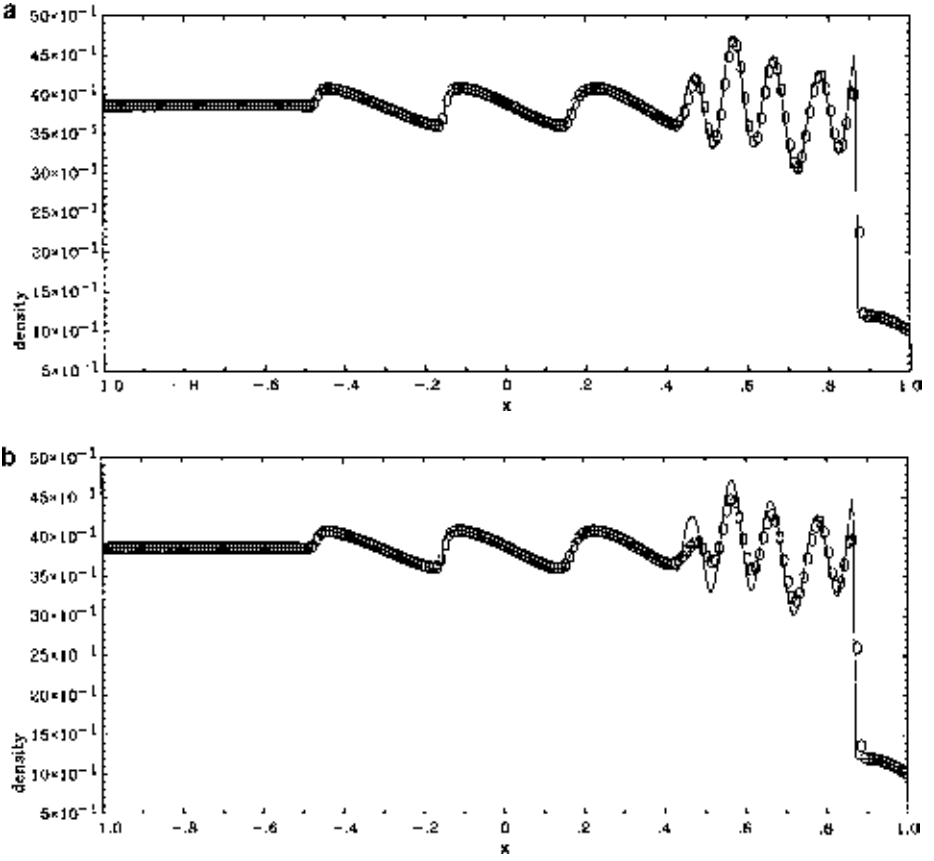
FIG. 5. The densities from the shock–entropy wave test problem. (a) The $r = 5$ MPWENO scheme run on a grid with 200 zones. We also ran the $r = 5$ MPWENO scheme on a grid of 800 zones in order to generate a reference calculation. The density from the reference calculation is shown as a solid line. (b) A similar plot for the $r = 3$ WENO scheme run on a grid with 200 zones. The ACM was not used. The problem was run with a CFL number of 0.6.

scheme run on a grid with 200 zones. As before, the solid line is the density from the reference calculation. Velocity and pressure variables are not shown because they are not as illustrative as the density variable. We see that the density from the $r = 5$ MPWENO scheme has converged to the reference calculation. Each of the extrema in the 200 zone calculation that was carried out with the $r = 5$ MPWENO scheme matches those in the reference calculation. On observing the extrema in Fig. 5a we see that there are no more than 11 points between the density extrema that immediately follow the shock. Thus the scheme has not just converged to the reference calculation but has done so with a very small number of points between extrema. In Section IV we pointed out not only that higher-order schemes converge faster than lower-order schemes but also that when the number of available points is kept fixed the higher-order scheme produces a smaller error. The ability of the $r = 5$ MPWENO scheme to converge to the reference calculation with just 11 points between extrema gives us a validation of the results in Section IV on a real-world problem. Figure 5b shows that the $r = 3$ WENO scheme has not converged to the reference calculation. In fact the extrema in Fig. 5b fall well short of those in the reference calculation. This clearly demonstrates that the theoretical results from the convergence tests that were carried out in

Section IV have a genuine bearing on real-world calculations. This also shows that there is a utility in using a scheme with very high order of accuracy. The $r = 3$ WENO scheme does converge to the reference calculation when run on a 400-zone grid. But this calculation, even though it is a one-dimensional calculation, is much more than twice as computationally expensive as a calculation that uses $r = 5$ MPWENO on a grid of 200 zones. With increasing dimensionality the computational costs favor the $r = 5$ MPWENO scheme even more. This clearly shows that in going from $r = 3$ WENO to $r = 5$ MPWENO we have not reached a point of diminishing returns. This also shows that when the calculation is starved of resolution or when complex flow structures develop on all scales (both of which occur in several turbulence calculations) the higher-order schemes do indeed give us a substantial advantage.

VII. MULTIDIMENSIONAL TESTS

VII.a. *Mach 3 Wind Tunnel with a Forward Facing Step*

This test problem was initially proposed and discussed in some detail by Woodward and Colella [49]. More recently it has been simulated at very high resolution by Cockburn and Shu [12]. Their simulation captured fine details in the solution, such as the vortex sheet rollup, which appear when the resolution and the accuracy of the numerical scheme are simultaneously increased. Our purpose is not to make such a resolution study but rather to validate the robust and accurate behavior of the schemes proposed here. For this reason we have simulated this test problem at the same resolution as Woodward and Colella [49]. The problem consists of a wind tunnel that is initialized on a two-dimensional grid with 240×80 zones that span the region $[0, 3] \times [0, 1]$. A forward facing step is set up with the corner of the step at (0.6, 0.2). The left boundary is initialized as an inflow boundary that has a Mach 3 gas with density of 1.4 and unit pressure flowing in. The gas has a ratio of specific heats given by 1.4. The right boundary is taken to be an outflow boundary. Reflective boundary conditions are applied to the walls of the tunnel. We treated the singularity at the corner with the same technique suggested in Woodward and Colella [49]. The problem was run until a simulation time of 4.0.

Figures 6a and 6b show the density and entropy at the final time. The problem was run with the $r = 5$ MPWENO scheme with $d^{MD}_{j+1/2} = d^{LC}_{j+1/2} = d^{M4}_{j+1/2}$. A CFL number of 0.6 was used. The RF version of the numerical flux was used. Since we wanted to test the basic scheme's ability to handle contact discontinuities in multiple dimensions without added embellishments we did not use the ACM. We see that all the shocks have sharp profiles which are properly captured on the computing grid. The vortex sheet that emanates from the Mach stem is properly resolved with just a few zones across the vortex sheet. This is made most evident in Fig. 6b for the entropy. It is significant that this scheme shows little or no spreading of the vortex sheet over the length of the computational domain despite the fact tha no ACM steepening was used.

VII.b. *Double Mach Reflection of a Strong Shock*

This test problem was also initially proposed and discussed in some detail by Woodward and Colella [49]. More recently it has been simulated at very high resolution by Cockburn and Shu [12]. Their simulation captured fine details in the solution, such as the rollup of
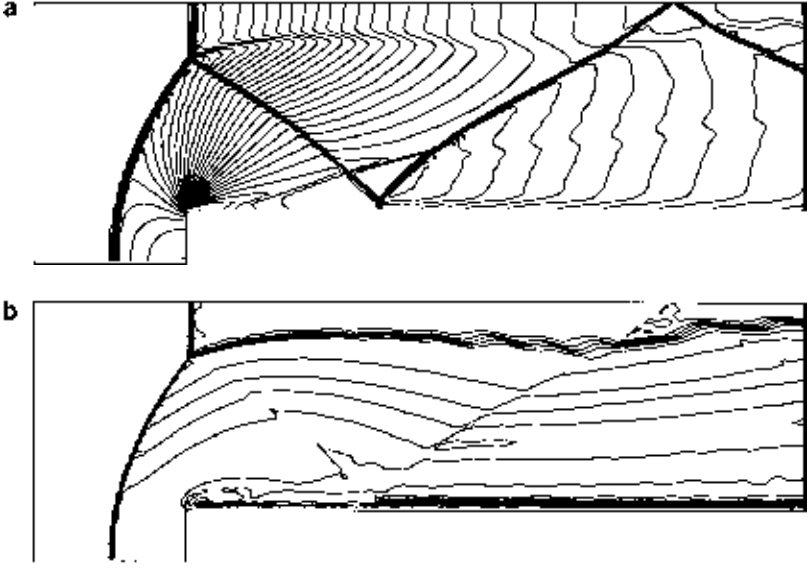
FIG. 6. (a) and (b) The density and entropy for the Mach 3 wind tunnel test problem. We used the $r = 5$ MPWENO scheme with the RF strategy for the fluxes. The ACM was not used. The problem was run with a CFL number of 0.6 and the results are shown at a simulation time of 4. The grid resolution was 240×80 zones. Some of the contours on the top boundary of the step show corruption of the contour lines; this is entirely an artifact of the plotting routines.

the contact discontinuity that emanates from the stronger of the two Mach stems, which appear when the resolution is increased. Our purpose is not to make such a resolution study but rather to validate the accuracy and robustness of the schemes proposed here. For this reason we have simulated this test problem at the same resolution as Woodward and Colella [49]. The problem is initialized on a two-dimensional grid with 480×120 zones that span the region $[0, 4] \times [0, 1]$. Only the region $[0, 3] \times [0, 1]$ is displayed in the figures. A right-moving Mach 10 shock is set up such that the shock front makes an angle of $60°$ with the x-axis and intersects the x-axis at $x = 1/6$. The boundary with $x > 1/6$ on the x-axis is taken to be a reflecting boundary. The ratio of specific heats was taken to be 1.4. The unshocked fluid has a density of 1.4 and a pressure of unity. The problem was run till a simulation time of 0.2 was reached.

Figures 7a and 7b show the density, pressure, entropy, and Mach number at the final time. The problem was run with the $r = 5$ MPWENO scheme with $d_{j+1/2}^{MD} = d_{j+1/2}^{LC} = d_{j+1/2}^{M4}$. A CFL number of 0.6 was used. The LLF version of the numerical flux was used. As shown by Cockburn and Shu [12] and Burger and Colella [8] this problem is genuinely under-resolved at the resolutions being used here. This is a situation where the ACM can help capture phenomena with the minimal number of zones possible. Thus to demonstrate that the ACM strategy works well in multiple dimensions we used the ACM technique for this problem. We see that both Mach stems are properly captured and all the shocks in the problem have crisp profiles. The boundaries of the dense jet that forms at the wall are properly captured. The rollup of the slip lines that emanate from the head of the jet is well captured in this simulation and is consistent with the higher-resolution simulations of Cockburn and Shu [12] and Burger and Colella [8]. This rollup of the slip lines shows through most clearly in the entropy plot; see Fig. 7b. This same problem has been done
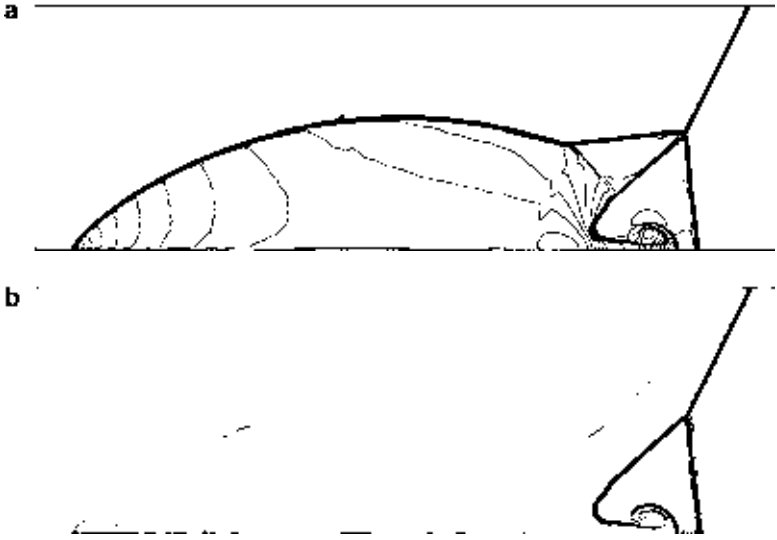
FIG. 7. (a) and (b) The density and entropy for the double Mach reflection test problem. We used the $r = 5$ MPWENO scheme with the LLF strategy for the fluxes. The ACM was used. The problem was run with a CFL number of 0.6 and the results are shown at a simulation time of 0.2. The grid resolution was 480×120 zones.

with the $r = 3$ WENO scheme in Jiang and Shu [23] using the same resolution as was used here. By comparing with that work we can see clearly that our use of the higher-order $r = 5$ MPWENO scheme here has had a positive effect on the quality of the solution.

A note needs to be added about the use of the RF numerical flux for this test problem. On using the RF version of the numerical flux we found a mild "carbuncle effect" at the point where the right-going normal shock meets the wall. The carbuncle effect—and causes that give rise to it—has been thoroughly discussed by Quirk [31]. Quirk found that this effect was essentially a consequence of poor coupling of the postshock entropy in the zones behind a shock when the shock is aligned with the grid. By comparing Eq. (2.5) with Eq. (2.6) it is easy to see that the LLF numerical flux gives better coupling between zones than the RF numerical flux. Thus the use of the LLF numerical flux in regions that are flagged to be in the immediate vicinity of shocks was seen to cure this carbuncle effect and restore good and stable behavior to the RF version of this scheme. As a result we were able to repeat this same test problem with the $r = 5$ MPWENO scheme without the carbuncle effect when the LLF flux was used in the vicinity of shocks but the RF flux was used everywhere else. It is also worthwhile to point out that, unlike other strategies that have been proposed for removing the carbuncle effect, this strategy does not degrade in any way the high-order accuracy of the scheme.

VII.c. *Shock–Vortex Interaction Problem*

In this third multidimensional test problem we study the interaction of a vortex with a shock. This test problem was first presented in Pao and Salas [29]. It was later carried out using a TVD scheme by Meadows *et al.* [28] and an $r = 3$ WENO scheme by Jiang and Shu [23]. The latter used exact expressions for the vortex while earlier authors had used approximate expressions for the vortex. We have used the same parameters for the shock

and the vortex as Jiang and Shu [23] with an important difference. All the previous authors have simulated this test problem with the flow aligned with one of the principal directions of the grid. We have chosen to have the shock normal make an angle of $45°$ to the x-axis. We also choose to have the vortex flow into the shock with a mean flow that makes an angle of $45°$ to the x-axis. Done this way it has a greater correspondence with real-world problems where one scarcely has the luxury of choosing grids that are aligned with the flow. The present test problem is a good model for sound waves that are generated when turbulence interacts with shock structures in a jet plume resulting in broadband noise. The more detailed interaction of shock waves with turbulence has also been studied in Jamme *et al.* [22] and so it is to be expected that the test problem described here plays a role in those simulations, too. The problem was initialized on a two-dimensional domain spanning $[0, 1.5] \times [0, 1.5]$ using a uniform grid of 150×150 zones. A standing Mach 1.1 shock was initialized along the line $y = -x + 1$ with the preshocked gas flowing into the shock from the left-bottom corner. The zones with $y \le -x + 1$, including the boundary zones that satisfy this condition, were initialized with preshocked gas. The zones with $y > -x + 1$, including the boundary zones that satisfy this condition, were initialized with postshocked gas. The imposition of these somewhat more complicated boundary conditions produced a slight corruption of the interior flow due to the boundaries but the effect was not very strong. We wanted to prevent strong startup transients from developing at the shock front. As a result, the primitive variables in the zones that were within a distance Δx of the line $y = -x + 1$ were given a linear variation that went from the preshock values to the postshock values. The gas had a ratio of specific heats given by 1.4. The preshocked gas had its density and pressure set to unity. A vortex centered at $(x_c, y_c) = (0.25, 0.25)$ was initialized so that its velocity, temperature, and entropy fluctuations to the mean flow in the fluid that was flowing into the shock were given by

$$(\delta v_x, \, \delta v_y) = \varepsilon \tau e^{\alpha(1-\tau^2)} (\sin\theta, \, -\cos\theta)$$

$$\delta T = -\frac{(\gamma-1)\varepsilon^2}{4\alpha\gamma} e^{2\alpha(1-\tau^2)}; \qquad \delta S = 0,$$

(7.1)

where $\tau = r/r_c$ and $r^2 = (x - x_c)^2 + (y - y_c)^2$. Here r_c denotes the core radius for the vortex, α controls the length scale over which the vortex decays, and ε denotes the vortex's strength so that we have $r_c = 0.05$, $\alpha = 0.204$, and $\varepsilon = 0.3$. The temperature and entropy are defined here as $T = P/\rho$ and $S = P/\rho^\gamma$. The problem was run until a simulation time of 0.8.

We used the $r = 5$ MPWENO scheme with $d_{j+1/2}^{\text{MD}} = d_{j+1/2}^{\text{LC}} = d_{j+1/2}^{\text{M4}}$ to simulate this test problem. The LLF version of the numerical fluxes was used. The ACM was not used. The problem was run with a CFL number of 0.6. Figures 8a and 8b show the density and Mach number, respectively, for the shock–vortex interaction test problem at a simulation time of 0.28. The vortex is halfway through the shock so that the vortex core is strongly interacting with the shock. Two distinct pressure regions are seen to develop in the postshock region. The region above the vortex center has higher pressure than the region below the vortex center. Figures 8c and 8d show the same two variables at a simulation time of 0.5. The vortex core has passed through the shock. A wave front that is centered on the vortex core has developed and is still strongly interacting with the shock. Figures 8e and 8f show the same two variables at a simulation time of 0.8. By this point the wave front emanating from the vortex core has reached the top boundary of the computational domain. The times 0.28, 0.5, and 0.8 in our simulation correspond approximately to times 0.2,
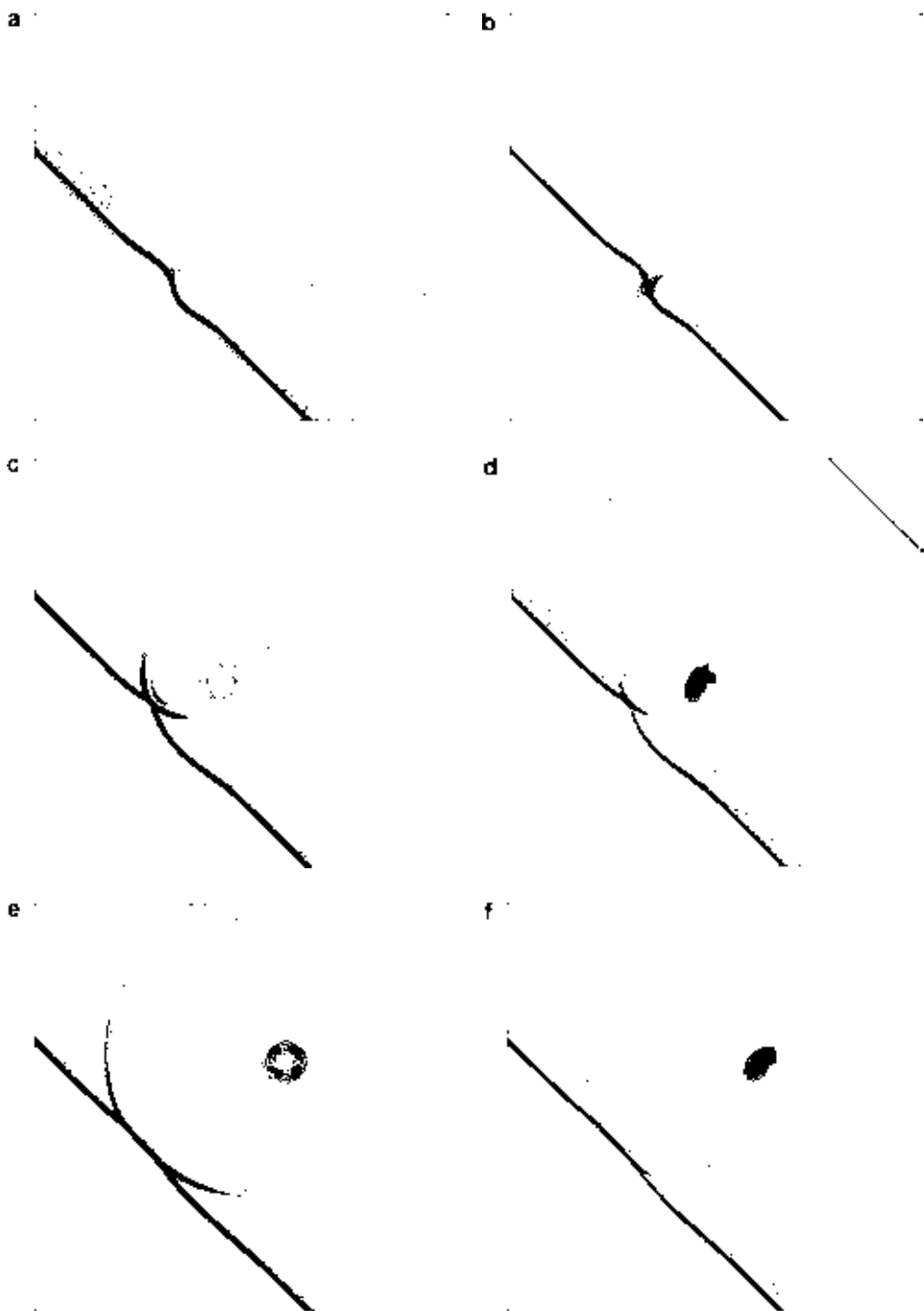
FIG. 8. (a) and (b) The density and Mach number, respectively, for the shock vortex interaction test problem at a simulation time of 0.28. (c) and (d) The density and Mach number in the same simulation at a time of 0.5. (e) and (f) The same two variables at a simulation time of 0.8. We used the $r = 5$ MPWENO scheme with the LLF strategy for the fluxes. The ACM was not used. The problem was run with a CFL number of 0.6. The grid resolution was 150×150 zones. The same simulation was run again using a PPMDE scheme again with a CFL number of 0.6 on a 150×150 zone grid. (g) and (h) The same two variables as (a) and (b) for the PPM scheme. (i) and (j) show the same two variables as (c) and (d) for the PPM scheme. (k) and (l) show the same two variables as (e) and (f) for the PPM scheme.
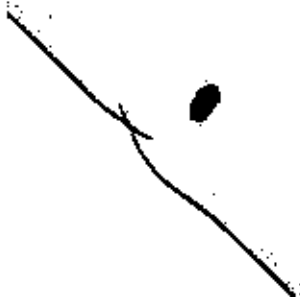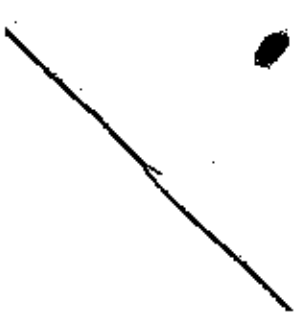
g

h

i

j

k

l

FIG. 8—*Continued*

0.35, and 0.6 in the simulation of Jiang and Shu [23]. We see that despite the modest resolution in the simulation that we have carried out here, the vortex still has a well-defined circular shape, thus showing that our scheme has accurately represented the shock–vortex interaction. We also see that despite the fact that the obliquely positioned shock has undergone strong interaction with the vortex, its structure has been properly preserved. We also wish to make a comparison with older, dimensionally split TVD schemes. For this reason, the problem was initialized on a similar grid of 150×150 zones and simulated with the PPMDE scheme of Colella and Woodward [13]. A Lapidus viscosity with the value suggested in Colella and Woodward [13] was used to provide multidimensional coupling. The steepener was not used. The flattening algorithm described in Colella and Woodward [13] was also not used because the shock described here is not very strong. The use of the flattening algorithm is only recommended for simulations with strong shocks. Its use here would only have degraded the order of accuracy with which the PPM scheme would have simulated this test problem. Figures 8g to 8l correspond to Figs. 8a to 8f, respectively. We see that there is considerable corruption of the density variable when the vortex core reaches the shock in Figs. 8g and 8h. Also when the wave front reaches the shock in Figs. 8i and 8j the multidimensional interaction of two waves produces considerable small scale fluctuation in the region where the shock and the wave front interact. We see, therefore, that on strongly multidimensional problems where the mean flow is not aligned with any of the grid directions the schemes presented here do indeed outperform the older, dimensionally split TVD schemes.

VIII. CONCLUSIONS

Based on the work presented in this paper we offer the following conclusions:

(1) We have designed a class of numerical schemes with increasingly high order of accuracy.

(2) The higher-order WENO schemes may not always preserve monotonicity. However, the monotonicity preserving bounds of Suresh and Huynh [45] restore monotonicity preserving behavior to these schemes. We call such schemes MPWENO schemes.

(3) The resulting schemes are robust and efficient, and can run with a reasonably large CFL number. To give an estimate of the efficiency, the $r = 5$ MPWENO scheme has a computational complexity that is only greater than the $r = 3$ WENO scheme by a factor of 1.35 to 1.5 on all problems that we have tried. The $r = 3$ WENO scheme, in turn, has a computational complexity that is only a factor of two larger than that of a TVD scheme.

(4) The higher-order members of the MPWENO family of schemes are almost spectrally accurate. We verify that this is so for MPWENO schemes with $r \geq 5$ by presenting several one- and two-dimensional convergence tests.

(5) We have examined the role of steepening algorithms such as the ACM algorithm of Yang [50]. We have documented suitable values for the parameters that are to be used in the ACM method with MPWENO schemes of increasingly high order. We were able to show that such algorithms do not damage the order property of the numerical method. We also show that higher-order schemes need to rely much less, or perhaps not at all, on such steepening algorithms.

(6) We have presented an extensive body of tests in one and two dimensions. These tests have shown conclusively that the higher-order schemes designed here have substantial advantages over lower-order schemes such as TVD schemes.

(7) We have shown that the methods developed here extend very well to other hyperbolic systems such as MHD.

(8) It is argued that the methods designed here have great utility in situations where the flow has complex structures on all scales. Applications that have this property may be found in DNS and LES simulations of compressible turbulence.

(9) We have carried out several multidimensional test problems on grids where the flow is not aligned with one of the grid directions and compared them with problems where the flow is aligned with one of the grid directions. This has led us to the conclusion that it is very advantageous to design and use test problems for higher-order schemes where the flow is not aligned with any of the grid directions. In particular, the difference between earlier, dimensionally split TVD schemes and the schemes designed here becomes glaringly apparent when the flow and the grid are not aligned.

ACKNOWLEDGMENTS

REFERENCES

1. D. S. Balsara, Linearized formulation of the Riemann problem for adiabatic and isothermal magnetohydrodynamics, *Ap. J. Supp.* **116**, 119 (1998).

2. D. S. Balsara, Total variation diminishing algorithim for adiabatic and isothermal magnetohydrodynamics, *Ap. J. Supp.* **116**, 133 (1998).

3. D. S. Balsara, TVD scheme for relativistic MHD, submitted for publication.

4. D. S. Balsara and D. Spicer, A staggered mesh algorithm using higher order Godunov fluxes to ensure solenoidal magnetic fields in MHD simulations, *J. Comput. Phys.* **149**, 270 (1997).

5. D. S. Balsara, A. Pouquet, D. Ward-Thompson, and R. M. Crutcher, Numerical MHD studies of turbulence and star formation, in *Interstellar Turbulence*, edited by J. Franco and A. Caraminana (Cambridge Univ. Press, Cambridge, UK, 1998).

6. M. Brio and C. C. Wu, An upwind differencing scheme for the equations of MHD, *J. Comput. Phys.* **75**, 400 (1988).

7. G. L. Browning and H.-O. Kreiss, Comparison of numerical methods for the calculation of two dimensional turbulence, *Math. Comput.* **52**, 369 (1989).

8. M. Berger and P. Colella, Local adaptive mesh refinement for shock hydrodynamics, *J. Comput. Phys.* **82**, 64 (1990).

9. J. Casper, Finite-volume implementation of high-order essentially nonoscillatory schemes in two dimensions, *AIAA J.* **30**, 2829 (1992).

10. J. Casper, C.-W. Shu, and H. Atkins, Comparison of two formulations of high-order accurate essentially nonoscillatory schemes, *AIAA J.* **32**, 1970 (1994).

11. S. R. Chakravarthy and S. Osher, *Very High Order Accurate TVD Schemes*, AIAA Paper # 85-0363.

12. B. Cockburn and C.-W. Shu, The Runge–Kutta discontinuous Galerkin method for conservation laws. V. Multidimensional systems, *J. Comput. Phys.* **141**, 199 (1998).

13. P. Colella and P. R. Woodward, The piecewise parabolic method (PPM) for gas-dynamical simulations, *J. Comput. Phys.* **54**, 174 (1984).

14. R. Fedkiw, R. Aslam, T. Merriman, and S. Osher, A non-oscillatory Eulerian approach to interfaces in multimaterial flows, submitted for publication.

15. S. Ghosal, An analysis of the numerical errors in large-eddy simulations of turbulence, *J. Comput. Phys.* **125**, 187 (1996).

16. S. K. Godunov, *Mat. Sb.* **47**, 357 (1959).

17. A. Harten, The artificial compression method for computation of shocks and contact discontinuities. I. Single conservation laws, *Comm. Pure Appl. Math.* **30**, 611 (1977).

18. A. Harten, High resolution schemes for hyperbolic conservation laws, *J. Comput. Phys.* **49**, 357 (1983).

19. A. Harten, ENO schemes with subcell resolution, *J. Comput. Phys.* **83**, 148 (1989).

20. A. Harten, B. Engquist, S. Osher, and S. J. Chakravarthy, Uniformly high order essentially non-oscillatory schemes, III, *J. Comput. Phys.* **71**, 231 (1987).

21. W. D. Henshaw, H.-O. Kreiss, and L. G. Reyna, ICASE Report #88-8 (1988).

22. S. Jamme, F. Torres, and J. B. Cazalbou, AIAA Paper 97-2070 (1997).

23. G.-S. Jiang and C.-W. Shu, Efficient implementation of weighted ENO schemes, *J. Comput. Phys.* **126**, 202 (1996).

24. P. D. Lax, Weak solutions of nonlinear hyperbolic equations and their numerical computation, *Comm. Pure Appl. Math.* **7**, 159 (1954).

25. B. P. Leonard, A. P. Lock, and M. K. MacVean, The NIRVANA scheme applied to one-dimensional advection, *Int. J. Num. Meth. Heat Fluid Flow* **5**, 341 (1995).

26. M. Lesieur and P. Comte, Large eddy simulations of compressible turbulent flows, in *Cours AGARD-VKI, Turbulence in Compressible Flows* (1997).

27. X.-D. Liu, S. Osher, and T. Chan, Weighted essentially nonoscillatory schemes, *J. Comput. Phys.* **115**, 200 (1994).

28. K. R. Meadows, A. Kumar, and M. Y. Hussaini, *A Computational Study of the Interaction between a Vortex and a Shock Wave*, AIAA Paper 89–1043 (1989).

29. S. P. Pao and M. D. Salas, AIAA Paper 81-1205 (1981).

30. D. H. Porter, P. R. Woodward, and A. Pouquet, Inertial range structures in decaying compressible trubulence flows, *Phys. Fluids* **10**, 237 (1998).

31. J. Quirk, A contribution of the great Riemann solver debate, *Int. J. Numer. Meth. Fluids* **18**, 555 (1994).

32. A. Rogerson and E. Meiberg, A numerical study of the convergence properties of ENO schemes, *J. Sci. Comput.* **5**, 151 (1990).

33. P. L. Roe, Approximate Riemann solvers, parameter vectors, and difference schemes, *J. Comput. Phys.* **43**, 357 (1981).

34. P. L. Roe, Some contributions to the modelling of discontinuous flows, in *Lect. in Appl. Math.* edited by B. Engquist, S. Osher, R. J. Somerville (Amer. Math. Soc., 1985), Vol. 22.

35. P. R. Roe, Discrete models for the numerical analysis of time-dependent multidimensional gas dynamics, *J. Comput. Phys.* **63**, 458 (1988).

36. P. L. Roe and D. S. Balsara, Notes on the eigensystem of magnetohydrodynamics, *SIAM J. Num. Anal.* **56**, 57 (1996).

37. D. Ryu and T. Jones, Numerical MHD in astrophysics: algorithm and tests for one-dimensional Flow, *Ap. J.* **442**, 228 (1995).

38. C.-W. Shu and S. J. Osher, Efficient implementation of essentially non-oscillatory shock capturing schemes, *J. Comput. Phys.* **77**, 439 (1988).

39. C.-W. Shu and S. J. Osher, Efficient implementation of essentially non-oscillatory shock capturing schemes II, *J. Comput. Phys.* **83**, 32 (1989).

40. C.-W. Shu, Numerical experiments on the accuracy of ENO and modified ENO schemes, *J. Sci. Comput.* **5**, 127 (1990).

41. C.-W. Shu, Essentially non-oscillatory and weighted essentially non-oscillatory schemes for hyperbolic conservation laws, in *Advanced Numerical Approximation of Nonlinear Hyperbolic Equations*, edited by B. Cockburn, C. Johnson, C.-W. Shu, and E. Tadmor (Editor-in-Chief: A. Quarteroni), (Springer, 1998), p. 325. [Lecture Notes in Mathematics, Vol. 1697.]

42. C.-W. Shu, T. A. Zang, G. Erlebacher, D. Whitaker, and S. Osher, High order ENO schemes applied to two- and three-dimensional compressible Flow, *Appl. Numer. Math.* **9**, 45 (1992).

43. G. A. Sod, A survey of finite difference methods for systems of nonlinear hyperbolic conservation laws, *J. Comput. Phys.* **27**, 1 (1978).

44. G. Strang, On the construction and comparison of difference schemes, *SIAM J. Numer. Anal.* **5**, 506 (1968).

45. A. Suresh and H. T. Huynh, Accurate monotonicity preserving scheme with Runge–kutta time-stepping, *J. Comput. Phys.* **136**, 83 (1997).

46. P. K. Sweby, High resolution schemes using flux limiters for hyperbolic conservation laws, *SIAM J. Num. Anal.* **21**, 995 (1984).

47. E. Tadmor, Numerical viscosity and the entropy condition for conservative difference schemes, *Math. Comput.* **43**, 369 (1984).

48. B. vanLeer, Towards the ultimate conservative difference scheme. V. A second order sequel to Godunov's method, *J. Comput. Phys.* **32**, 101 (1979).

49. P. Woodward and P. Colella, The numerical simulation of two-dimensional fluid flow with strong shocks, *J. Comput. Phys.* **54**, 115 (1984).

50. H. Yang, An artificial compression method for ENO schemes, the slope modification method, *J. Comput. Phys.* **89**, 125 (1990).